Size-dependent mass absorption cross-section of soot particles from various sources

Corbin, Joel C.; Johnson, Tyler J.; Liu, Fengshan; Sipkens, Timothy A.; Johnson, Mark P.; Lobo, Prem; Smallwood, Greg J.

Publisher's version / Version de l'éditeur:
https://doi.org/10.1016/j.carbon.2022.02.037
Carbon, 192, C, pp. 438-451, 2022-03-03

Size-dependent mass absorption cross-section of soot particles from various sources

Joel C. Corbin[1,*], Tyler J. Johnson[2], Fengshan Liu[1], Mark P. Johnson[3], Prem Lobo[1], Greg J. Smallwood[1]

[1]*Metrology Research Centre, National Research Council Canada, Ottawa, Ontario, Canada*

[2]*Atmose Ltd, Edmonton, Alberta, Canada*

[2]*Rolls Royce plc, Derby, UK*

Corresponding author: tel 613-993-2176, Joel.Corbin@nrc-cnrc.gc.ca

Draft prepared for Carbon

Last modified 2021-07-04

Graphical abstract

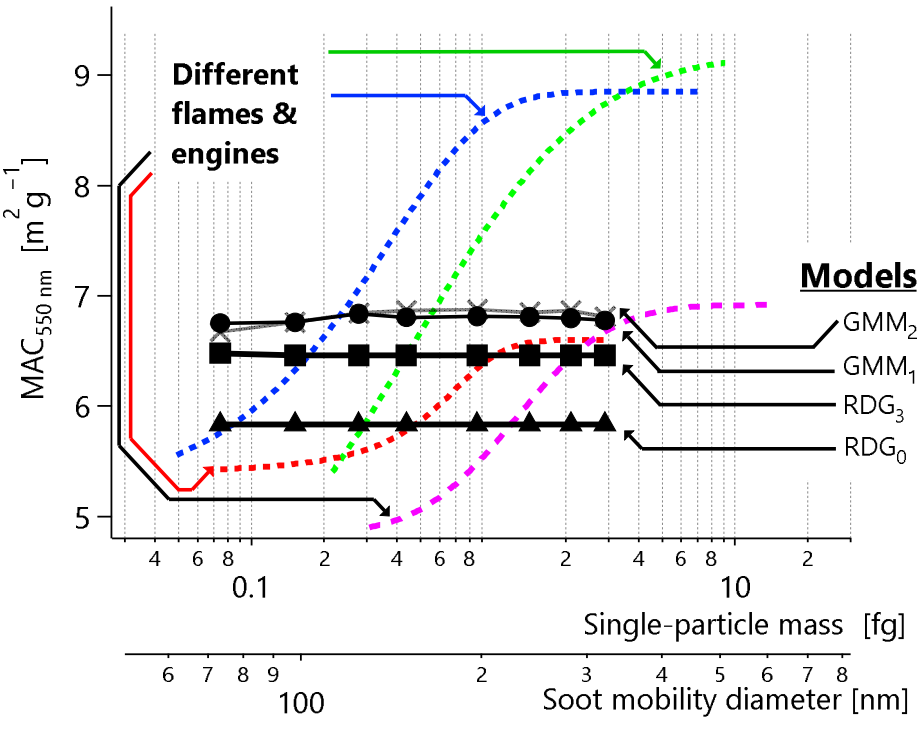

1. Abstract

The mass absorption cross-section (MAC) of combustion-generated soot is used in pollution and emissions measurements to quantify the mass concentration of soot and in atmospheric modelling to predict the radiative effects of soot on climate. Previous work has suggested that the MAC of soot particles may change with their size, due to (1) internal scattering among monomers in the soot aggregate, (2) the correlation of soot primary-particle diameter with aggregate size, (3) quantum confinement effects, or (4) a size-dependent degree of soot graphitization. Here, we report a size-dependent MAC for ex-situ soot sampled from two commercially available diffusion-flame soot generators, one aviation turbine engine, and one diesel generator. We also incorporate literature data. We show that the MAC increases with aggregate size until a plateau is reached at single particle masses between 4 and 30 fg (approximately 300–650 nm soot mobility diameter). Moreover, we show that models of hypotheses (1), (2), and (3) do not describe our measurement results, leaving hypothesis (4) as the only remaining candidate. Considering the polydispersity of real world soot sources, the size-dependent MAC may lead to a difference of approximately 10% between the smallest and largest particles emitted by a given soot source.

2. Introduction

The incomplete combustion of hydrocarbon fuels often results in the nucleation and growth of carbonaceous soot particles. These flame-generated nanoparticle aggregates of graphitized carbon spherules are highly light-absorbing; consequently, they play a major role in the radiative balance of the Earth [1] and in heat transfer in combustion [2]. Soot's light absorption is also commonly exploited for its measurement [3] since soot particles generally dominate total light absorption by atmospheric aerosol particles [4] and often also in flames [5]. Conversely, soot's absorption properties are often used to predict its radiative effects from gravimetric or chemical measurements [1]. Therefore, accurate measurements and predictions of the impacts of the soot emitted from combustion require a thorough understanding of the factors influencing soot's light absorption.

Soot particles can also be called black carbon (BC) [1,6] or soot BC [7] to emphasize their strong broadband light absorption. In contexts such as regulatory measurements, soot particles are measured as non-volatile particulate matter (nvPM). Other forms of BC also exist, such as the carbonized fuel droplets or cenospheres often called char [7]. Soot particles are not purely composed of graphitized carbon; they contain approximately 2–10 % oxygen and a small amount of hydrogen in the form of refractory surface functional groups [8–11] and a smaller amount of metallic elements due to refractory metal compounds (ash) [12,13]. Some complexity is introduced by volatiles such as volatile organic compounds (VOCs) which often condense onto soot particles; these VOCs are not considered to be part of the soot particle [6] as they exist in a dynamic equilibrium with the gas phase.

Light absorption by soot particles at wavelength λ is often quantified by the mass absorption cross-section (MAC_λ): the absorption coefficient of a population of particles normalized to their mass concentration. Unlike the refractive index (RI) or absorption function $E(m)$, which must be retrieved through model fits, MACs can be determined directly from measurements [14]. The MAC of soot aggregates may be influenced by their morphology [15–18] and degree of graphitization [19].

The MAC may also be enhanced by coatings of non-absorbing materials such as VOCs [20–22]; this enhancement is complicated by the possibility of soot restructuring during VOC condensation.

Although comprehensive reviews of the typical MAC of soot have focussed on measurements with no size classification [14][23,24], size-dependent soot MACs have been measured in four previous studies. Dastanpour et al. [25] reported a size dependence of the MAC of soot particles produced by a large, inverted diffusion flame. They described this dependence using a power-law fit of MAC versus single- particle mass (m_{p}). Forestieri et al. [26] also observed a size-dependent MAC in a compiled laboratory data set of diffusion-flame soot. They found that a Rayleigh-Debye-Gans (RDG) model (which treats soot spherules as non-interacting primary particles) overpredicted the MAC of smaller aggregates ($x < 0.9$) but could adequately represent larger ones. They developed an empirical description of the MAC of smaller aggregates based on Mie theory (which treats aggregated soot spherules as volume-equivalent spheres) with an empirically fitted RI. Finally, Khalizov et al. [27] and Kholghy and DeRosa [28] also observed size-dependent MACs for diffusion-flame and flame-spray-pyrolysis soot, respectively. Two other studies have reported size-dependent MAC values for mature soot [29,30] but only measured large particles (with mass m_{p} >>1 fg) in the regime where negligible size dependence has been observed (Section 4.1.). Although most of these studies classified particles by mass rather than size, we use the term size here due to the fundamental importance of the size parameter $\left(x = \pi d_{pp}/\lambda, \text{where } d_{pp} \text{ is the monomer diameter}\right)$ in nanoparticle optics.

RDG and Mie models are the simplest models of soot MAC. Mie models represent the entire soot aggregate as a volume-equivalent sphere and cannot describe the size-dependent MAC accurately [26]. RDG models are more accurate, but employ the assumption of negligible internal scattering between aggregate monomers [31]. This assumption can be refined by introducing an RDG correction factor h (Section 3.1.) derived from accurate numerical methods such as generalized multiparticle Mie (GMM) theory, the T-matrix method, or the discrete dipole

approximation. The h factor quantifies the influence of internal scattering on the soot MAC. By definition, h is 1.0 for a single monomer. For a typical monomer diameter $d_{pp} = 15$ nm, h increases to a plateau at $h \approx 1.2$ for an aggregate composed of a moderate number of monomers ($10^1 < N_{pp} < 10^2$) in point contact, then decreases again for larger aggregates $\left(N_{pp} > 10^2\right)$ [31]. We note that these values are all sensitive to the size parameter *x*, the RI, and on the assumption of an aggregate morphology defined by diffusion-limited cluster aggregation (DLCA) [31].

Optical models can also be used to quantify the influence of other details of soot structure on MAC, in addition to internal scattering. For example, Dastanpour et al. [25] observed a correlation between monomer size (d_{pp}) and aggregate size, and discussed its possible influence on MAC which can be readily modelled. Dastanpour et al. also measured a size-dependent soot maturity based on particle mobility diameter d_m, for $125 < d_m < 300$ nm particles using Raman spectroscopy [25,32] and attributed their observed size-dependent MAC to this trend. A quantitative model for the evolution of soot maturity in flames was subsequently described by Kelesidis and Pratsinis [33]. That model incorporated the quantum confinement effects identified by Wang and co-workers [34] for incipient soot particles in premixed flames ($4 < d_m < 23$ nm), thereby parameterizing the refractive-index-dependent absorption function $E(m)$ in terms of d_m via the electronic band gap E_g [33]. This maturity model is independent of the internal scattering and monomer-aggregate size correlation hypotheses.

In addition to the above effects, the effects of monomer polydispersity and necking and overlap between monomers on aggregate absorption or MAC have also been investigated. The former effect (polydispersity of d_{pp}) has a negligible influence on the MAC of DLCA soot monomers in point contact [35,36]. The latter effect (necking and overlap) also has only a small predicted influence on soot MAC, affecting h by less than 10% in studies which modelled soot morphology phenomenologically, based on electron micrographs [17], or mechanistically,

based on in-flame soot formation processes [37]. Necking and overlap substantially affect h only for incipient soot particles with mobility diameter $d_m < 50$ nm, because surface growth (which is the driving force behind overlap and necking) become less important during the later stages of soot evolution [33]. A 50 nm small soot emitted from a flame would be more mature [38] due to processes such as oxidation and annealing [39]. Overall, in mature soot, polydispersity and surface growth are unlikely to have a major influence on the soot MAC. We therefore focus our following discussion on the effects of aggregate internal scattering, monomer-aggregate size correlation, and quantum confinement, which were hypothesized as potential causes of a size-dependent soot MAC.

In this work, we have measured a range of size-dependent MACs for soot from two commercial soot generators, one aviation turbine engine, and one diesel generator. We used various instruments to quantify absorption coefficients. We used a centrifugal particle mass analyzer (CPMA) to classify particles by mass-to-charge ratio and an electrometer to quantify total charge and therefore total mass. To interpret the CPMA setpoints in terms of average-single-particle-mass (or equivalent size), we performed a data inversion based on the CPMA transfer function and verified this analysis using two additional data processing approaches. We discuss our measurements in the context of similar literature measurements, as well as in the context of numerical models representing the relevant size-dependent phenomena discussed above.

3. Methods

3.1. Samples

<Table 1 here>

Four different soot sources were used in this work, an Argonaut miniature inverted soot generator (MISG), a Jing miniCAST model 5201c burner, a Gnome

aviation turbine engine, and a diesel generator (Honda, Model EX4D, operated at 89% of maximum sustainable load) (Table 1). The MISG is an inverted diffusion flame and was operated with air and propane flows of 7.5 standard litres per minute (SLPM) and 0.0625 SLPM, respectively. Unpublished measurements by our laboratory, using the same technique described below, have shown that the MAC of soot produced by the MISG is insensitive to these flows, and also insensitive to fuel composition. Therefore, only a single MISG setpoint was used in this study.

<Table 2 here>

The miniCAST produces soot from a quenched diffusion flame. In contrast to the MISG, the MAC of soot produced by the miniCAST has been directly observed to vary with combustion-gas flow [40] as suggested by changes in related physical parameters [41–43]. We therefore operated the miniCAST at the three setpoints shown in Table 2. Setpoints D and S represent mature soot with a high degree of graphitization according to previous measurements in the literature [40,44]. Setpoint A mimics the conditions used to calibrate the Micro Soot Sensor plus (MSS) for aviation turbine engine non-volatile particulate matter emissions measurements.

<Figure 1 here>

Emissions from all the soot sources were sampled using heated lines (60 °C) and diluted with room-temperature air upstream of the catalytic stripper. In some cases, dilution factors were as low as 2 to ensure that signals were measurable at the smallest particle sizes, but high enough to prevent water condensation in the sampling lines. Further details of the sampling configuration for the Gnome turbine engine at the Rolls-Royce facility in Derby, UK are available in Ref. [45]. The general laboratory setup for the measurements performed at the NRC has been described previously [46].

193 ### 3.1. Soot characterization

194 Scanning mobility particle sizers (SMPSs; TSI Inc., USA) were used to characterize
195 the size distributions of the non-volatile particles measured downstream of a
196 350 °C catalytic stripper (CS015, Catalytic Instruments GmbH, Germany). The
197 results are summarized in Table 1 in terms of the measured count median
198 diameter (CMD) and geometric standard deviation (GSD). The mass median
199 diameter (MMD) calculated from these properties [47] is also included. We also
200 report the primary particle diameters in terms of $d_{pp,100}$ (the mean primary
201 particle diameter of $d_m = 100$ nm aggregates) from literature for the Gnome [45]
202 and Argonaut MISG [32] sources. For the miniCAST, no $d_{pp,100}$ measurements were
203 available and we quote instead the d_{pp} reported by Ref. [40] for setpoint D,
204 although this value was reported without reference to aggregate size. We expect
205 that the miniCAST d_{pp} is biased high (i.e., represents the mean primary particle
206 diameter of aggregates with $d_m > 100$ nm, instead of $d_m = 100$ nm as assumed)
207 considering the normal operator bias towards larger particles and the shift of the
208 aggregate size distribution towards larger sizes.
209

210 ### 3.2. Mass absorption cross-section (MAC) measurements

211 The MAC of a population of particles [units: $\mathrm{m^2 g^{-1}}$] is evaluated as

$$\mathrm{MAC}_\lambda = \frac{B_{\mathrm{abn},\lambda}}{M_{\mathrm{PM}}}, \qquad 1$$

212 where MAC_λ is the MAC measured at wavelength λ, $B_{\mathrm{abn},\lambda}$ is the absorption cross
213 section at wavelength λ, and M_{PM} is the particulate matter (PM) mass
214 concentration. M_{PM} represents the soot mass concentration, since we measured
215 non-volatile PM from the combustion of hydrocarbon fuels with negligible metal
216 and sulphur content.

217 Since we used various instruments to measure $B_{\mathrm{abn},\lambda}$ at different λ, we followed
218 Refs. [1,14,23] in converting our MAC measurements to a 550 nm ($\mathrm{MAC}_{550\mathrm{nm}}$) as
219

$$\mathrm{MAC}_{550\mathrm{nm}} = \mathrm{MAC}_{\lambda}\left(\frac{550\mathrm{nm}}{\lambda}\right)^{-\mathrm{AAE}} \quad (2)$$

and assuming an absorption Ångström exponent (AAE) of 1. Our procedure for MAC measurements is summarized in the following subsections and in Table S1.

3.3. CERMS measurements of M_{PM}

We measured M_{PM} using the CPMA-Electrometer Reference Mass Standard (CERMS) [46,48–50] shown in Figure 1. In the CERMS, sample particles are highly charged by a unipolar diffusion aerosol charger (UDAC, Cambustion, UK) before being transmitted to a centrifugal particle mass analyzer (CPMA, Cambustion, UK). The fraction of uncharged particles exiting the UDAC was verified to be negligible in a dedicated experiment using an electrostatic precipitator (ESP, Cambustion, UK) and condensation particle counter (CPC, TSI 3776, USA) in series.

During M_{PM} measurement, charged particles flow through the CPMA, which transmits particles of a known mass-to-charge ratio (m_q/q) to an electrometer and a challenge instrument, where m_q is the mass of a single particle with charge q. Particles with m_q/q greater or smaller than the CPMA setpoint are removed by electrical or centrifugal forces. The electrometer measures the total current (I) of the CPMA-classified particles, which for a known volumetric flow rate Q through the electrometer allows M_{PM} to be calculated as [48]:

$$M_{\mathrm{PM}} = \frac{m_1 I}{Qe} \quad (3)$$

where m_1 is the mass of a singly-charged particle and e is the elementary charge. This M_{PM} may be used to calibrate instruments reporting mass concentration [46,49], or can be used to calculate MAC if the challenge instrument measures $B_{\mathrm{abn},\lambda}$. Based on our previous work [46], we considered data where the electrometer measured less than 250 fA as inaccurate.

3.1. *Measurements of $B_{abn,\lambda}$*

We used and calibrated three different instruments to measure $B_{\mathrm{abn},\lambda}$ (Table S1). We used a CAPS PM_{SSA} monitor (Aerodyne Research Inc., USA), which measures the lifetime of photons in an optical cell to derive the aerosol extinction coefficient $B_{\mathrm{ext},\lambda}$ while an integrating nephelometer simultaneously measures the aerosol light scattering coefficient $B_{\mathrm{sca},\lambda}$ from the same cell. The difference, extinction minus scattering, is then the absorption coefficient. The $B_{\mathrm{ext},\lambda}$ measurement is calibration-free with an estimated accuracy of 5 % [51]. The $B_{\mathrm{sca},\lambda}$ measurement is calibrated by reference to the $B_{\mathrm{ext},\lambda}$ measurement using non-absorbing particles with diameters at least a factor of 3 smaller than the measurement wavelength [52]. Truncation uncertainty in the CAPS PM_{SSA} nephelometer is negligible for the sizes measured here [52] and the overall uncertainty in $B_{\mathrm{abn},\lambda}$ is estimated as approximately 10 % [52,53]. In this study, we size-classified non-absorbing $(NH_4)_2SO_4$ particles with an aerodynamic diameter of 290 nm (corresponding to an approximate mobility and spherical-equivalent diameter of 200 nm) using an Aerodynamic Aerosol Classifier (AAC, Cambustion, UK) and a measurement wavelength of 660 nm.

The other two instruments used in this study were both photoacoustic spectrometers which periodically laser-heat particles in an acoustic resonator to generate pressure waves that are proportional to $B_{\mathrm{abn},\lambda}$ in magnitude. A microphone measures these pressure waves. The photoacoustic extinctiometer (PAX, Droplet Measurement Technologies Inc., USA) uses an 870 nm diode laser and reports $B_{\mathrm{abn},\lambda}$ as well as M_{eBC} by applying Equation 1 with an assumed MAC_{870nm} of 4.74 $m^2\ g^{-1}$ (derived from MAC_{550nm} of 7.5 $m^2\ g^{-1}$ and AAE of 1.0).

The PAX is calibrated in two steps using two additional detectors, a laser power meter and a light-scattering detector. The laser power meter allows $B_{\mathrm{ext},\lambda}$ to be calculated at extremely high values ($> 10^4$/Mm) using the Beer-Lambert law. For non-absorbing particles, $B_{\mathrm{ext},\lambda} = B_{\mathrm{sca},\lambda}$. Thus, the first calibration step uses a high concentration of $(NH_4)_2SO_4$ particles to define $B_{\mathrm{sca},\lambda}$ using the Beer-Lambert law. In

the second calibration step, the $(NH_4)_2SO_4$ is replaced with a high concentration of absorbing particles (we used Aquadag colloidal graphite) for which $B_{\mathrm{ext},\lambda} = B_{\mathrm{sca},\lambda} + B_{\mathrm{abn},\lambda}$. Since $B_{\mathrm{ext},\lambda}$ is known from the Beer-Lambert law and $B_{\mathrm{sca},\lambda}$ is known from the first step, a reference value of $B_{\mathrm{abn},\lambda}$ may be calculated and used to calibrate the PAX microphone. Overall, this two-step PAX calibration requires the assumption that the instrument behaves linearly from $> 10^4$/Mm down to the normal measured range (≈ 10/Mm); an assumption that was recently verified experimentally [46].

The MSS (AVL, Austria) is a photoacoustic spectrometer similar to the PAX, but uses an 808 nm laser and does not incorporate additional calibration detectors. Instead, it is calibrated by taking filter samples in parallel to the instrument. Either the gravimetric mass or the elemental carbon mass (EC, determined by thermal-optical analysis) on the filters is then used as a calibration reference, depending on whether the calibration is intended for use in the aviation sector (EC) or not (gravimetric). Thus, in the aviation sector the MSS-reported mass represents M_{eBC} calibrated to M_{EC} and also represents the assumption that the MAC of the calibration source and measured sample are equal. The difference between not M_{PM} and M_{PM} is discussed in detail in [46]. The assumption that the MAC did not change is often reasonably accurate mature soot [14,23], but not for the present work. Here, we transformed the M_{eBC} reported by the MSS into $B_{\mathrm{abn,808nm}}$ by using the MAC of the Argonaut MISG as a reference as follows. First, the $\mathrm{MAC}_{870\mathrm{nm}}$ of MISG soot was measured at NRC using the PAX and converted to $\mathrm{MAC}_{808\mathrm{nm}}$ using an AAE of 1. Then, the Argonaut MISG M_{PM} was measured using the CERMS, and finally Equation 1 was applied to calculate the $B_{\mathrm{abn,808nm}}$ measured by the MSS+. Our assumption that the Argonaut MISG MAC was constant is justified by literature reviews of soot in general [14,23] and by Argonaut-MISG-specific measurements performed in our laboratory [54].

3.2. MAC data analysis

In our experiments, the CPMA classifies particles of a given mass-to-charge ratio m_q/q. Particles are classified with a user-specified resolution $R_m = m_1/\Delta m$, where m_1 is mass-to-charge setpoint for a singly charged particle and Δm is the width in particle mass space of the transfer function. If all particles are singly charged then $q = 1$ and the mean single-particle mass is simply m_1. However, if doubly-charged particles ($q = 2$) are introduced into the CPMA, then the mean single-particle mass is the number-weighted mean of m_1 and m_2. The same is true for all multiply charged particles ($q > 1$) present in substantial numbers. This issue must be addressed by calculating the number and charge distribution of particles entering the CPMA (a two-dimensional matrix) in order to determine the number and charge distribution of CPMA-classified particles. Similar data inversions are routinely used to measure size distributions with SMPSs [55] or electrical mobility spectrometers (EMSs) such as the Cambustion DMS500 [56], which uses the same unipolar charger as used in this study. We performed this conventional data inversion to estimate the average mass m_p of CPMA-transmitted particles. We also performed a more complex system-of-equations approach to account for the potential difference of MAC in particles of different masses due to differences in their charge. Finally, we additionally performed a simpler iterative-average-charge approach for cross-validation. Because all three approaches gave consistent results (Figure S1 and Section S1.2), we chose to focus on the results of the conventional data inversion. Further details are given in Section S1.2 and Figure S1, Figure S2, Figure S3, and Figure S4.

3.1. MAC modelling

<Table 3 here>

We modelled the MAC of soot using Mie, RDG, and GMM approaches to reproduce the literature hypotheses and models discussed in the Introduction. The inputs to

the models are summarized in Table 3 and described in the following. The models are simplified whenever possible due to the computational burden of the most precise (GMM) calculations.

Our initial model represented the aviation turbine engine soot described in Table 1 with $m = 1.66 + 0.76i$ [33], soot density $\rho = 1800$ kg m^{-3} [57], and $d_{pp,100} =$ 20 nm [45]. We converted the mass of soot particles to d_m using the following formulation of the universal soot effective-density relationship [58]:

$$d_m = (100\text{ nm})\left(\frac{m_p}{0.2670\text{ fg}}\right)^{1/2.48} \quad (4)$$

where 0.2670 fg is the mass of a 100 nm mobility diameter soot particle with effective density 510 ± 8 kg m^{-3} [58].

For Mie calculations, we used this d_m as the particle size (*Mie model; used for literature context only*). For RDG calculations, we used d_{pp} as the particle size (*RDG-0 model*). According to the RDG approximation,

$$\text{MAC}_{\lambda,\text{RDG}} = h \cdot \frac{6\pi E(m)}{\lambda\rho} \quad (5)$$

where the absorption function $E(m) = \text{Imag}[(m^2 - 1)/(m^2 + 1)\,]$, ρ is the particle density, λ the light wavelength, and $h = \text{MAC}_{\lambda,\text{accurate}}/\text{MAC}_{\lambda,\text{RDG}}$ the correction factor which scales the RDG MAC to the value predicted by accurate calculations.

To account for the effects of internal scattering within a soot aggregate on MAC (which leads to $h > 1$ for aggregates of relatively small to moderate sizes), we used the GMM method for aggregates formed by point-contact monomers with $d_{pp} =$ 20 nm as described previously [59] (*GMM-1 model*).

We also conducted GMM calculations for aggregates formed by monomers whose diameter increases with the aggregate size following the monomer-aggregate size

correlation (*GMM-2 model*) using Equation 9 of Olfert and Rogak [58]:

$$d_{pp} = \left(d_{pp,100}\right)\left(\frac{d_m}{100\ \text{nm}}\right)^{0.35} \quad (6)$$

where $d_{pp,100}$ was taken as 20 nm (Table 1).

To evaluate the quantum confinement and soot maturity effects on soot RI and ρ we used an RDG model (*RDG-3 model*) together with the E_g, m, and ρ parameterizations given by Kelesidis and Pratsinis [33]. We simplified the evaluation of these effects by using the RDG method because our GMM results indicated a negligible influence of aggregation over the range of modelled aggregate sizes.

4. Results and Discussion

4.1. Measured MAC from flames and engines

<Figure 2 here>

Figure 2 shows the dependence of MAC on single-particle mass (m_p) of soot produced by the Gnome aircraft turbine engine, the MISG (3 different absorption instruments), the miniCAST (3 different flame conditions), and the diesel generator. All of the data suggest that a plateau of MAC exists at ~ 4 fg < m_p < 30 fg (about $300 < d_m < 650$ nm, according to Equation 4) and that the MAC decreases below 4 fg. MAC is also likely to decrease above 30 fg based on Mie theory [23] or aggregate [31] models, but this is outside the scope of our discussion; we focus on the most commonly observed soot sizes.

The data in Figure 2 span all m_p for which M_PM signals were above the 250 fA limit of detection for the CERMS noted above. Therefore, the data illustrate the MAC of all single-particle masses m_p (or sizes) for which substantial integrated mass M_PM was present. This is illustrated by the shaded curves in the lower part of Figure 2, which approximately represent the mass distributions of the Gnome aircraft turbine engine (grey) and the miniCAST-A (blue) samples. These approximate

mass distributions were calculated by transforming the lognormal mobility size distribution parameters in Table 1 to mass distributions using the universal mass-mobility relationship of Olfert and Rogak [58].

The functional form of the data in Figure 2 is not well constrained by our measurements. The aircraft turbine engine data suggest a sigmoidal function (such as Equation S6) but with variation in the inflection point and slope. This point is discussed further below.

4.2. Impact of size-dependent MAC on overall MAC of lognormal distributions

Soot sources generally produce polydisperse, lognormally distributed mobility-size or mass distributions. The size dependence of polydisperse soot with MAC would be smoother than that of the mass-classified soot shown in Figure 2, since the CPMA output represents a narrower range of sizes than a polydisperse distribution. Moreover, this size dependence would be negligible for distributions where most of the particulate mass was found in larger particles with $m_p > 4$ fg (approximately > 160 nm volume-equivalent diameter or $d_m > 350$ nm). For most of our samples, the mass median diameters (MMDs) of 400 nm to 500 nm indicate a minor influence of the size-dependent MAC on the mass-weighted integral MAC. Note that for an MMD of 400 nm and GSD of 1.6, 84% of the integrated lognormal mass is found in particles larger than MMD ÷ GSD = 250 nm [47], i.e., in the upper plateau region of Figure 2. In contrast, the aviation turbine engine and diesel generator have smaller MMDs of 110 nm and 190 nm, respectively. These MMDs fall in the region where the size dependence of MAC is the strongest in Figure 2. Therefore, measurements of such engine emissions which report M_{PM} by assuming a constant MAC (Equation 1) may introduce a size-dependent bias due to the size-dependent MAC.

Our assumed GMDs of 40 nm and 100 nm for aviation turbine engine and Diesel generator soot are both above the midpoint of the range of sizes expected for such

engines, particularly for modern engines. A recent review of aviation turbine soot [60] reported a range of GMDs from 15 nm to 60 nm, with smaller particles measured at lower thrust settings (<40% of maximum). GMDs for automotive gasoline-direct-injection (GDI) or port-fuel-injection (PFI) engines are similarly small, with vehicle models since the year 2008 having GMDs from 10 to 70 nm (mean of type approval cycle data) [61]. (For earlier years, the reported GMDs were progressively larger, up to a maximum of 100 nm.) Approximately half of the soot from such engines would be expected to fall close to the midpoint of the various size-dependent MACs shown in Figure 2.

<Figure 3 here>

The exact influence of the size-dependent MAC on the size-integrated MAC of an aerosol depends not only on the size-dependent MAC but also on the aerosol size distribution. We illustrate this in Figure 3 for the measured Gnome engine MACs and for a variety of GMDs. The Gnome engine MACs were parameterized using a sigmoidal fit to the Gnome turbine engine data in Figure 2. The integrated MAC_{550nm} was obtained by weighting the size-dependent MAC function by a simple lognormal soot size distribution at the GMDs given by the abscissa and the GSDs given by the labels on the graph. For the small soot particles from the Gnome turbine engine, the uncertainty introduced by our simple lognormal representation is expected to be negligible [62]. The figure also plots the GMDs reported previously and discussed above.

For GMDs of 10 nm to 100 nm and reasonable GSDs, the size-integrated MAC spans almost the entire range measured for the size-resolved MAC. From the upper plateau to the lower plateau, the calculated MAC_{550nm} for the integrated size distribution decreases 18% from the plateau value of 6.6 $m^2 g^{-1}$ to 5.4 $m^2 g^{-1}$. For the more limited range of GMDs emitted by a single engine, a range closer to 10% might be expected. This 10% is comparable in magnitude to the 9% standard deviation of recently reported size-integrated MACs in the literature [14], but represents a measurement bias rather than an uncertainty. For example, to our knowledge, no previous measurements have been capable of distinguishing this

change in MAC since the accepted techniques for measuring aviation turbine engine soot all measure M_{PM} using techniques that are sensitive to changes in MAC. Such previous measurements therefore lacked an independent reference, such as the CERMS used in our work.

4.1. Literature comparison

<place Figure 4 here>

Figure 4 places our measurements in the context of the previous size-resolved MAC measurements from diffusion flames (Figure 4a,b,c) or internal combustion engines(Figure 4d,e). The literature data all show a trend similar to our data, despite combining various experimental techniques. For example, Dastanpour et al. [25] classified particles by mass-to-charge ratio using a CPMA (similar to our work) while the other studies classified particles by mobility-to-charge ratio using differential mobility analyzers (DMAs). Other differences in particle charge, charge correction approaches, and light-absorption measurements are summarized in Table S2. This variety of experimental approaches reduces the likelihood that experimental bias caused the observed trends.

All of the studies reported in the literature may be described by the sigmoidal function mentioned above, although most studies do not report a broad enough range of sizes to differentiate between this sigmoidal function and simpler alternatives (e.g. quadratic or power-law). In particular, the study by Khalizov et al. [27] measured only three different particle sizes and the study by Kholghy and DeRosa [28] measured five.

Dastanpour et al. [25] specifically discussed a size-dependent MAC for inverted-diffusion-flame soot and postulated a power-law fit of MAC to m_p. Our new data and our compilation of literature data clearly show that this dashed blue line is a

poor description of the overall trend for the size-dependent MAC of soot. We also note that Dastanpour et al.'s fit was strongly influenced by the high outliers (light-blue inverted triangles shown in Figure 4e) which were measured when the flame fuel was mixed with N_2, uniquely different from all other measurements plotted. We excluded this N_2-diluted flame soot data set and re-fit the data (blue triangles shown in Figure 4e) using the sigmoidal Equation S6 (dashed blue line in Figure 4e) to illustrate consistency with the sigmoidal trend described above for aviation turbine engine soot.

The study of Forestieri et al. [26] is also consistent with our interpretation. That study compiled data from four separate studies performed over the course of 7 years; we therefore plotted bars (upper and lower quartiles, with symbols for the median) rather than points in Figure 4d. Nevertheless, their results, representing measurements at 405 nm, 532 nm, and 630 nm, are fully consistent with the discussion above. While there is some apparent wavelength dependence to the trend, it is secondary to the MAC–size trend. Finally, two other studies reporting size-resolved MAC measurements by Cross et al. [30] and You et al. [29] focussed on particles with $m_p \gg 1$ fg and thus did not observe the sigmoidal trends discussed here.

The variability between our reported measurements of different soot sources is much smaller than the variability between studies of similar sources (e.g. the laboratory diffusion flames in Figure 4b and Figure 4d; and the inverted flames in Figure 4a and Figure 4e; see Figure S6 for a single plot overlaying these data). From this observation, it is inferred that the variability in calibration accuracy is likely an important influencing factor in the MACs reported in the literature. Therefore, the most reliable estimates of the typical value of soot MAC may be from reviews of MAC measurements made in multiple laboratories, such as [23,24]. Furthermore, when overlaid (as shown in Figure S6), the combined measurements display variability not only in the value of MAC but also in the rate of change of MAC with size, suggesting that the observed MAC–size trends vary between sources.

4.2. *MAC models and hypothetical causes of size-dependent MAC*

Figure 4f shows the modelled MAC results described in Section 3.1. and Table 3. The models represent three different literature hypotheses which might produce a size-dependent soot MAC (1–aggregate internal scattering; 2–correlation between monomer and aggregate size; 3–quantum confinement effects; see Introduction). The figure also includes a null-hypothesis RDG model numbered 0 (which excludes all 3 of the above hypotheses) and a Mie model, which is used for context in the following discussion. Figure 4f is reproduced in Figure S5 with an additional axis illustrating the number of primary particles in each modelled soot aggregate.

The Mie model in Figure 4f (grey open circles and dotted line) is a simple model representing the soot aggregate as a volume-equivalent sphere. It is the only model to predict a size dependent MAC, but does not capture the MAC plateau at $m_p > 1$ fg nor the rapid decrease in MAC at smaller sizes. The limitations of Mie theory in describing soot optics are well known [23,63] and the Mie model is not included as a hypothetical explanation for the observed size-dependent MAC. Rather, the Mie model in Figure 4f was included because Forestieri et al. [26] proposed that a Mie approach may be empirically useful if the soot RI is treated as a fitting parameter at small size parameters ($x < 0.9$). Our observed variability in the MAC as a function of combustion source shows that this approach cannot accurately represent size-resolved MACs unless done on a source-specific basis.

The RDG model (black open circles and dashed line) in Figure 4f represents the simplistic assumption of non-interacting soot primary particles. This model has no size-dependent parameters and therefore shows no size dependence. This RDG model represents the null hypothesis where none of the three literature hypotheses are represented and serves as a point of reference for the other models.

In contrast to the RDG model, the GMM–DLCA model (Figure 4f, GMM-1, black filled circles and solid line), accounts for primary-particle interactions within a DLCA soot aggregate. The GMM–DLCA modelled MAC is 14% higher than the RDG model (h = 1.14), but also shows negligible size dependence across our range of interest ($\Delta\, h < 0.011$). Thus, there is a negligible size dependence of modelled MAC on d_m in our measured range.

Our modelled h can be compared to the h predicted by Kelesidis et al. [37], who modelled soot particles in greater morphological detail than our model of point-contact spheres. As mentioned in the introduction, they modelled surface growth and therefore necking and overlap between monomers. They reported a parameterization of h with d_m describing their modelled particles. However, their parameterization also does not predict a substantial size dependence of h in our measured size range; using their parameterization, we calculated $1.19 < h < 1.22$ for the Gnome aviation turbine engine soot particles. This suggests a negligible (~5%) influence of monomer overlap on the MAC of soot aggregates formed by point-contact monomers in our observed size range, consistent with the conclusions of previous modelling work [17,64].

Parameterizing the correlation of d_{pp} with d_m (grey line in Figure 4f) within a GMM model (Figure 4f, GMM-2, solid grey line) also yielded negligible size dependence across our range of interest. The parameterization changed the range of N_{pp} for the Gnome aviation turbine engine data set from 9 to 332, to 19 to 159 (Figure S5). Therefore, we rejected the hypothesis that this correlation may explain the MAC size-dependence.

The final model in Figure 4f explores the influence of soot composition by parameterizing the soot RI and density following Kelesidis and Pratsinis [33], whose work built on that of Wang and coworkers [34] by considering the optical band gap E_g. With this quantum confinement model (Figure 4f, RDG-3, black open square circle and dashed line), our parameterized m and ρ spanned narrow ranges ($1.66 + 0.75i$ to $1.66 + 0.76i$, and 1613 to 1625 kg m^{-3}), so our modelled MAC

573 spanned narrow ranges. The quantum confinement model results were not
574 substantially altered by setting $\rho = 1800$ kg m^{-3} or by using d_{pp} from Equation 6 in
575 place of d_m. For the quantum confinement model to display a strongly size-
576 dependent soot MAC, we would need to reformulate the $m = m(E_g)$ or $E_g = E_g(d_m)$
577 parameterizations of Kelesidis and Pratsinis [33]. As was the case with the
578 approach of Forestieri et al. [26], the observed variability in size dependence
579 between sources creates challenges for this approach.
580
581 Thus, none of the effects of internal scattering, monomer-aggregate size
582 correlation, or quantum confinement, can explain the size dependence of MAC we
583 have observed in this study and corroborated with the literature results. As noted
584 in the introduction, the additional hypothesis of monomer overlap or necking has
585 already been excluded in previous studies. A second additional hypothesis is that
586 the soot particles studied have restructured to more compact morphologies than
587 DLCA would predict. This hypothesis can be rejected based on the weak size
588 dependence of our Mie model results, which represented the extreme compactness
589 of an equivalent-volume sphere. Indirect insight into this hypothesis is also gained
590 from our measurements of single-scattering albedos (SSAs), as discussed in
591 Section S1.4, Figure S7, and Figure S8.
592
593 Therefore, according to the process of elimination, the only remaining hypothesis
594 that may explain the measured size-dependent MAC is that the degree of
595 graphitization of soot is size dependent in a manner that is dependent on the
596 combustion source.
597

598 *4.3. Implications for CPMA-electrometer (CERMS) calibrations*

599 Recent studies have discussed the calibration of black-carbon or soot instruments
600 using an experimental configuration identical to that discussed here, and referred
601 to as the CPMA-Electrometer Reference Mass Standard (CERMS) [46,48–50]. We
602 have used an identical setup in our experiments. Our identification of a size-
603 dependent MAC shows that the CPMA setpoint may slightly influence the

calibration result obtained from CERMS. However, this influence is relatively minor if calibration is performed at a range of CPMA setpoints. For example, if the Gnome aviation turbine engine data presented in Figure 2 are treated as calibration data (all sizes), the calibration residuals are only scattered about the regression line by < 10% (Figure S9). This scatter is an extreme example, since in practice, a CERMS calibration should not equally weight data taken at the tails of the size distribution.

5. Conclusions

We measured the relationship between MAC and soot particle mass for mature soot from four different combustion sources. With decreasing particle mass, we observed that the MAC decreases from an upper plateau of approximately 8 $m^2 g^{-1}$ at roughly 4 fg (about 300 nm mobility diameter) to a minimum value of at least 4 $m^2 g^{-1}$ at smaller masses/sizes. The general trends we observed are consistent with previous literature measurements, but the size dependent MAC appears to vary between combustion sources. Taken together with the literature measurements, the data suggest that the decrease from the MAC upper plateau may vary in its starting point and rate of decrease between sources.

When the size-dependent (or, equivalently, mass-dependent) MAC is weighted by the soot mass distribution (cf. shaded curves in Figure 2), the resulting average MAC will be affected most strongly by the small particles produced by internal combustion engines such as the Gnome aviation turbine engine measured here. Aviation turbine engines and automotive GDI and PFI engines produce significantly smaller soot particles than other sources, with GMDs in the range 10 nm to 70 nm, such that the size-integrated MAC may fall within the range of most rapidly changing size-dependent MAC. This shift in MAC can lead to significant biases in the reported BC or nvPM mass concentrations of absorption-based instruments.

We modelled soot MAC using different methods and various hypotheses from the

633 literature which may potentially explain the size-dependent soot MAC: aggregation
634 effects (h), monomer-aggregate size correlation ($d_{pp} \propto d_m$), and changing
635 composition ($E_g \propto d_m$ and $\rho \propto d_m$ according to literature parameterizations).
636 None of these hypotheses reproduced the observed size-dependent MAC. By
637 eliminating the alternative hypotheses, we conclude that the size-dependent MAC
638 indicates a size-dependent degree of graphitization which varies between
639 combustion sources for reasons which have not yet been adequately described.
640 Future work should seek to parameterize this dependence in terms of easily
641 measured flame conditions.
642

643 ## 6. Acknowledgements

644 Technical support from Daniel Clavel and Simon-Alexandre Lussier (in situ
645 measurements) and Brett Smith (microscopy images) is greatly appreciated. We thank the
646 Rolls-Royce team at Derby for their support. We are grateful to Andrew Crayford at Cardiff
647 University for providing the MSS, Hongsheng Guo and Shouvik Dev for providing the diesel
648 generator and Hamed Nikookar for discussion.
649

650 ## 7. Author contributions

651 Conceptualization – JCC, GJS, PL, FL; Investigation – JCC, GJS, MPJ, PL; Formal
652 analysis – JCC, TJJ, FL; Methodology – JCC, GJS, TJJ, FL,MPJ, PL; Writing original
653 draft – JCC; Writing review and editing – all authors.
654

655 ## 8. References

656 [1] T.C. Bond, S.J. Doherty, D.W. Fahey, P.M. Forster, T. Berntsen, B.J. DeAngelo,
657 M.G. Flanner, S. Ghan, B. Kärcher, D. Koch, S. Kinne, Y. Kondo, P.K. Quinn, M.C.
658 Sarofim, M.G. Schultz, M. Schulz, C. Venkataraman, H. Zhang, S. Zhang, N.
659 Bellouin, S.K. Guttikunda, P.K. Hopke, M.Z. Jacobson, J.W. Kaiser, Z. Klimont,
660 U. Lohmann, J.P. Schwarz, D. Shindell, T. Storelvmo, S.G. Warren, C.S. Zender,
661 Bounding the role of black carbon in the climate system: A scientific

assessment, J. Geophys. Res. Atmos. 118 (2013) 5380–5552. https://doi.org/10.1002/jgrd.50171.

[2] I. Glassman, R.A. Yetter, Combustion, Academic Press, Burlington, MA, USA, 2008.

[3] H. Moosmüller, R.K. Chakrabarty, W.P. Arnott, Aerosol light absorption and its measurement: A review, J. Quant. Spectrosc. Radiat. Transf. 110 (2009) 844–878. https://doi.org/10.1016/j.jqsrt.2009.02.035.

[4] Y. Feng, V. Ramanathan, V.R. Kotamarthi, Brown carbon: A significant atmospheric absorber of solar radiation, Atmos. Chem. Phys. 13 (2013) 8607–8621. https://doi.org/10.5194/acp-13-8607-2013.

[5] H.A. Michelsen, Probing soot formation, chemical and physical evolution, and oxidation: A review of in situ diagnostic techniques and needs, Proc. Combust. Inst. 36 (2017) 717–735. https://doi.org/10.1016/j.proci.2016.08.027.

[6] H.A. Michelsen, M.B. Colket, P.-E. Bengtsson, A. D'Anna, P. Desgroux, B.S. Haynes, J.H. Miller, G.J. Nathan, H. Pitsch, H. Wang, A Review of Terminology Used to Describe Soot Formation and Evolution under Combustion and Pyrolytic Conditions, ACS Nano. 14 (2020) 12470–12490. https://doi.org/10.1021/acsnano.0c06226.

[7] J.C. Corbin, H. Czech, D. Massabò, F.B. de Mongeot, G. Jakobi, F. Liu, P. Lobo, C. Mennucci, A.A. Mensah, J. Orasche, S.M. Pieber, A.S.H. Prévôt, B. Stengel, L.-L. Tay, M. Zanatta, R. Zimmermann, I. El Haddad, M. Gysel, Infrared-absorbing carbonaceous tar can dominate light absorption by marine-engine exhaust, Npj Clim. Atmos. Sci. 2 (2019). https://doi.org/10.1038/s41612-019-0069-5.

[8] J.L. Figueiredo, M.F.R. Pereira, M.M.A. Freitas, J.J.M. Órfão, Modification of the surface chemistry of activated carbons, Carbon N. Y. 37 (1999) 1379–1389. https://doi.org/10.1016/S0008-6223(98)00333-9.

[9] G. Matuschek, E. Karg, A. Schröppel, H. Schulz, O. Schmid, Chemical investigation of eight different types of carbonaceous particles using thermoanalytical techniques, Environ. Sci. Technol. 41 (2007) 8406–8411. https://doi.org/10.1021/es062660v.

[10] J.C. Corbin, U. Lohmann, B. Sierau, A. Keller, H. Burtscher, A.A. Mensah, Black carbon surface oxidation and organic composition of beech-wood soot aerosols, Atmos. Chem. Phys. 15 (2015) 11885–11907. https://doi.org/10.5194/acp-15-11885-2015.

[11] M. Singh, R.L. Vander Wal, The role of fuel chemistry in dictating nanostructure evolution of soot toward source identification, Aerosol Sci. Technol. 54 (2020) 66–78.

https://doi.org/10.1080/02786826.2019.1675864.

[12] S. Gagné, M. Couillard, Z. Gajdosechova, A. Momenimovahed, G. Smallwood, Z. Mester, K. Thomson, P. Lobo, J.C. Corbin, Ash-Decorated and Ash-Painted Soot from Residual and Distillate-Fuel Combustion in Four Marine Engines and One Aviation Engine, Environ. Sci. Technol. (2021) acs.est.0c07130. https://doi.org/10.1021/acs.est.0c07130.

[13] T. Torvela, J. Tissari, O. Sippula, T. Kaivosoja, J. Leskinen, A. Virén, A. Lähde, J. Jokiniemi, Effect of wood combustion conditions on the morphology of freshly emitted fine particles, Atmos. Environ. 87 (2014) 65–76. https://doi.org/10.1016/j.atmosenv.2014.01.028.

[14] F. Liu, J. Yon, A. Fuentes, P. Lobo, G.J. Smallwood, J.C. Corbin, Review of recent literature on the light absorption properties of black carbon: Refractive index, mass absorption cross section, and absorption function, Aerosol Sci. Technol. 54 (2020) 33–51. https://doi.org/10.1080/02786826.2019.1676878.

[15] L. Liu, M.I. Mishchenko, Effects of aggregation on scattering and radiative properties of soot aerosols, J. Geophys. Res. 110 (2005). https://doi.org/10.1029/2004jd005649.

[16] B. V Scarnato, S. Vahidinia, D.T. Richard, T.W. Kirchstetter, Effects of internal mixing and aggregate morphology on optical properties of black carbon using a discrete dipole approximation model, Atmos. Chem. Phys. 13 (2013) 5089–5101. https://doi.org/10.5194/acp-13-5089-2013.

[17] J. Yon, A. Bescond, F. Liu, On the radiative properties of soot aggregates part 1: Necking and overlapping, J. Quant. Spectrosc. Radiat. Transf. 162 (2015) 197–206. https://doi.org/10.1016/j.jqsrt.2015.03.027.

[18] J.G. Radney, R. You, X. Ma, J.M. Conny, M.R. Zachariah, J.T. Hodges, C.D. Zangmeister, Dependence of Soot Optical Properties on Particle Morphology: Measurements and Model Comparisons, Environ. Sci. Technol. 48 (2014) 3169–3176. https://doi.org/10.1021/es4041804.

[19] T.C. Bond, Spectral dependence of visible light absorption by carbonaceous particles emitted from coal combustion, Geophys. Res. Lett. 28 (2001) 4075–4078. https://doi.org/10.1029/2001gl013652.

[20] L. Fierce, T.B. Onasch, C.D. Cappa, C. Mazzoleni, S. China, J. Bhandari, P. Davidovits, D. Al Fischer, T. Helgestad, A.T. Lambe, A.J. Sedlacek, G.D. Smith, L. Wolff, Radiative absorption enhancements by black carbon controlled by particle-to-particle heterogeneity in composition, Proc. Natl. Acad. Sci. 117 (2020) 5196–5203. https://doi.org/10.1073/pnas.1919723117.

[21] W.R. Heinson, P. Liu, R.K. Chakrabarty, Fractal scaling of coated soot aggregates, Aerosol Sci. Technol. 51 (2016) 12–19.

https://doi.org/10.1080/02786826.2016.1249786.

[22] G. Lefevre, J. Yon, M. Bouvier, F. Liu, A. Coppalle, Impact of Organic Coating on Soot Angular and Spectral Scattering Properties, Environ. Sci. Technol. 53 (2019) 6383–6391. https://doi.org/10.1021/acs.est.8b05482.

[23] T.C. Bond, R.W. Bergstrom, Light absorption by carbonaceous particles: An investigative review, Aerosol Sci. Technol. 40 (2006) 27–67. https://doi.org/10.1080/02786820500421521.

[24] F. Liu, J. Yon, A. Fuentes, P. Lobo, G.J. Smallwood, J.C. Corbin, Review of recent literature on the light absorption properties of black carbon: Refractive index, mass absorption cross section, and absorption function, Aerosol Sci. Technol. 54 (2020). https://doi.org/10.1080/02786826.2019.1676878.

[25] R. Dastanpour, A. Momenimovahed, K. Thomson, J. Olfert, S. Rogak, Variation of the optical properties of soot as a function of particle mass, Carbon N. Y. 124 (2017) 201–211. https://doi.org/10.1016/j.carbon.2017.07.005.

[26] S.D. Forestieri, T.M. Helgestad, A.T. Lambe, L. Renbaum-Wolff, D.A. Lack, P. Massoli, E.S. Cross, M.K. Dubey, C. Mazzoleni, J.S. Olfert, A.J. Sedlacek, A. Freedman, P. Davidovits, T.B. Onasch, C.D. Cappa, Measurement and modeling of the multiwavelength optical properties of uncoated flame-generated soot, Atmos. Chem. Phys. 18 (2018) 12141–12159. https://doi.org/10.5194/acp-18-12141-2018.

[27] A.F. Khalizov, H. Xue, L. Wang, J. Zheng, R. Zhang, Enhanced Light Absorption and Scattering by Carbon Soot Aerosol Internally Mixed with Sulfuric Acid, J. Phys. Chem. A. 113 (2009) 1066–1074. https://doi.org/10.1021/jp807531n.

[28] M.R. Kholghy, V.G. DeRosa, Morphology, composition and optical properties of jet engine-like soot made by a spray flame, Combust. Flame. 231 (2021) 111480. https://doi.org/10.1016/j.combustflame.2021.111480.

[29] R. You, J.G. Radney, M.R. Zachariah, C.D. Zangmeister, Measured Wavelength-Dependent Absorption Enhancement of Internally Mixed Black Carbon with Absorbing and Nonabsorbing Materials, Environ. Sci. Technol. 50 (2016) 7982–7990. https://doi.org/10.1021/acs.est.6b01473.

[30] E.S. Cross, T.B. Onasch, A. Ahern, W. Wrobel, J.G. Slowik, J. Olfert, D.A. Lack, P. Massoli, C.D. Cappa, J.P. Schwarz, J.R. Spackman, D.W. Fahey, A. Sedlacek, A. Trimborn, J.T. Jayne, A. Freedman, L.R. Williams, N.L. Ng, C. Mazzoleni, M. Dubey, B. Brem, G. Kok, R. Subramanian, S. Freitag, A. Clarke, D. Thornhill, L.C. Marr, C.E. Kolb, D.R. Worsnop, P. Davidovits, Soot Particle Studies--Instrument Inter-Comparison--Project Overview, Aerosol Sci. Technol. 44 (2010) 592–611. https://doi.org/10.1080/02786826.2010.482113.

[31] C.M. Sorensen, J. Yon, F. Liu, J. Maughan, W.R. Heinson, M.J. Berg, Light scattering and absorption by fractal aggregates including soot, J. Quant.

Spectrosc. Radiat. Transf. 217 (2018) 459–473. https://doi.org/10.1016/j.jqsrt.2018.05.016.

[32] A. Baldelli, S.N. Rogak, Morphology and Raman spectra of aerodynamically classified soot samples, Atmos. Meas. Tech. 12 (2019) 4339–4346. https://doi.org/10.5194/amt-12-4339-2019.

[33] G.A. Kelesidis, S.E. Pratsinis, Soot light absorption and refractive index during agglomeration and surface growth, Proc. Combust. Inst. 37 (2019) 1177–1184. https://doi.org/10.1016/j.proci.2018.08.025.

[34] K. Wan, X. Shi, H. Wang, Quantum confinement and size resolved modeling of electronic and optical properties of small soot particles, Proc. Combust. Inst. 38 (2021) 1517–1524. https://doi.org/10.1016/j.proci.2020.07.145.

[35] C. Liu, Y. Yin, F. Hu, H. Jin, C.M. Sorensen, The Effects of Monomer Size Distribution on the Radiative Properties of Black Carbon Aggregates, Aerosol Sci. Technol. 49 (2015) 928–940. https://doi.org/10.1080/02786826.2015.1085953.

[36] J. Yon, F. Liu, J. Morán, A. Fuentes, Impact of the primary particle polydispersity on the radiative properties of soot aggregates, Proc. Combust. Inst. 37 (2019) 1151–1159. https://doi.org/10.1016/j.proci.2018.07.065.

[37] G.A. Kelesidis, S.E. Pratsinis, Determination of the volume fraction of soot accounting for its composition and morphology, Proc. Combust. Inst. (2020). https://doi.org/10.1016/j.proci.2020.07.055.

[38] K.O. Johansson, F. El Gabaly, P.E. Schrader, M.F. Campbell, H.A. Michelsen, Evolution of maturity levels of the particle surface and bulk during soot growth and oxidation in a flame, Aerosol Sci. Technol. 51 (2017) 1333–1344. https://doi.org/10.1080/02786826.2017.1355047.

[39] M.L. Botero, Y. Sheng, J. Akroyd, J. Martin, J.A.H. Dreyer, W. Yang, M. Kraft, Internal structure of soot particles in a diffusion flame, Carbon N. Y. 141 (2019) 635–642. https://doi.org/10.1016/j.carbon.2018.09.063.

[40] L. Durdina, P. Lobo, M.B. Trueblood, E.A. Black, S. Achterberg, D.E. Hagen, B.T. Brem, J. Wang, Response of real-time black carbon mass instruments to mini-CAST soot, Aerosol Sci. Technol. 50 (2016) 906–918. https://doi.org/10.1080/02786826.2016.1204423.

[41] M.M. Maricq, Examining the Relationship Between Black Carbon and Soot in Flames and Engine Exhaust, Aerosol Sci. Technol. 48 (2014) 620–629. https://doi.org/10.1080/02786826.2014.904961.

[42] R.H. Moore, L.D. Ziemba, D. Dutcher, A.J. Beyersdorf, K. Chan, S. Crumeyrolle, T.M. Raymond, K.L. Thornhill, E.L. Winstead, B.E. Anderson, Mapping the Operation of the Miniature Combustion Aerosol Standard (Mini-{CAST})

817 Soot Generator, Aerosol Sci. Technol. 48 (2014) 467–479.
818 https://doi.org/10.1080/02786826.2014.890694.

819 [43] J.C. Corbin, B. Sierau, M. Gysel, M. Laborde, A. Keller, J. Kim, A. Petzold, T.B.
820 Onasch, U. Lohmann, A.A. Mensah, Mass spectrometry of refractory black
821 carbon particles from six sources: Carbon-cluster and oxygenated ions,
822 Atmos. Chem. Phys. 14 (2014) 2591–2603. https://doi.org/10.5194/acp-14-
823 2591-2014.

824 [44] M. Saffaripour, L.L. Tay, K.A. Thomson, G.J. Smallwood, B.T. Brem, L. Durdina,
825 M. Johnson, Raman spectroscopy and TEM characterization of solid
826 particulate matter emitted from soot generators and aircraft turbine
827 engines, Aerosol Sci. Technol. 51 (2017) 518–531.
828 https://doi.org/10.1080/02786826.2016.1274368.

829 [45] J.S. Olfert, M. Dickau, A. Momenimovahed, M. Saffaripour, K. Thomson, G.
830 Smallwood, M.E.J. Stettler, A. Boies, Y. Sevcenco, A. Crayford, M. Johnson,
831 Effective density and volatility of particles sampled from a helicopter gas
832 turbine engine, Aerosol Sci. Technol. 51 (2017) 704–714.
833 https://doi.org/10.1080/02786826.2017.1292346.

834 [46] J.C. Corbin, A. Moallemi, F. Liu, S. Gagné, J.S. Olfert, G.J. Smallwood, P. Lobo,
835 Closure between particulate matter concentrations measured ex situ by
836 thermal–optical analysis and in situ by the CPMA–electrometer reference
837 mass system, Aerosol Sci. Technol. 0 (2020) 1–17.
838 https://doi.org/10.1080/02786826.2020.1788710.

839 [47] W.C. Hinds, Aerosol technology: properties, behavior, and measurement of
840 airborne particles, John Wiley & Sons, 1999.

841 [48] J.P.R. Symonds, K.S.J. Reavell, J.S. Olfert, The {CPMA}-Electrometer
842 System{\textemdash}A Suspended Particle Mass Concentration Standard,
843 Aerosol Sci. Technol. 47 (2013) i--iv.
844 https://doi.org/10.1080/02786826.2013.801547.

845 [49] M. Dickau, T.J. Johnson, K. Thomson, G. Smallwood, J.S. Olfert, Demonstration
846 of the {CPMA}-Electrometer System for Calibrating Black Carbon Particulate
847 Mass Instruments, Aerosol Sci. Technol. 49 (2015) 152–158.
848 https://doi.org/10.1080/02786826.2015.1010033.

849 [50] J. Titosky, A. Momenimovahed, J. Corbin, K. Thomson, G. Smallwood, J.S.
850 Olfert, Repeatability and intermediate precision of a mass concentration
851 calibration system, Aerosol Sci. Technol. 53 (2019) 701–711.
852 https://doi.org/10.1080/02786826.2019.1592103.

853 [51] T.B. Onasch, P. Massoli, P.L. Kebabian, F.B. Hills, F.W. Bacon, A. Freedman,
854 Single Scattering Albedo Monitor for Airborne Particulates, Aerosol Sci.
855 Technol. 49 (2015) 267–279.
856 https://doi.org/10.1080/02786826.2015.1022248.

[52] R.L. Modini, J.C. Corbin, B.T. Brem, M. Irwin, M. Bertò, R.E. Pileci, P. Fetfatzis, K. Eleftheriadis, B. Henzing, M.M. Moerman, F. Liu, T. Müller, M. Gysel-Beer, Detailed characterization of the CAPS single-scattering albedo monitor (CAPS PMssa) as a field-deployable instrument for measuring aerosol light absorption with the extinction-minus-scattering method, Atmos. Meas. Tech. 14 (2021). https://doi.org/10.5194/amt-14-819-2021.

[53] J. Perim De Faria, U. Bundke, A. Freedman, T.B. Onasch, A. Petzold, Laboratory validation of a compact single-scattering albedo (SSA) monitor, Atmos. Meas. Tech. 14 (2021) 1635–1653. https://doi.org/10.5194/amt-14-1635-2021.

[54] A. Moallemi, M. Kazemimanesh, J.C. Corbin, K. Thomson, G. Smallwood, J.S. Olfert, P. Lobo, Characterization of black carbon particles generated by a propane-fueled miniature inverted soot generator, J. Aerosol Sci. 135 (2019) 46–57. https://doi.org/10.1016/j.jaerosci.2019.05.004.

[55] S.C. Wang, R.C. Flagan, Scanning Electrical Mobility Spectrometer, Aerosol Sci. Technol. 13 (1990) 230–240. https://doi.org/10.1080/02786829008959441.

[56] G. Biskos, K. Reavell, N. Collings, Description and Theoretical Analysis of a Differential Mobility Spectrometer, Aerosol Sci. Technol. 39 (2005) 527–541. https://doi.org/10.1080/027868291004832.

[57] F.-X.X. Ouf, S. Bourrous, S. Fauvel, A. Kort, L. Lintis, J. Nuvoli, J. Yon, True density of combustion emitted particles: A comparison of results highlighting the influence of the organic contents, J. Aerosol Sci. 134 (2019) 1–13. https://doi.org/10.1016/j.jaerosci.2019.04.007.

[58] J. Olfert, S. Rogak, Universal relations between soot effective density and primary particle size for common combustion sources, Aerosol Sci. Technol. 53 (2019) 485–492. https://doi.org/10.1080/02786826.2019.1577949.

[59] F. Liu, G.J. Smallwood, The effect of particle aggregation on the absorption and emission properties of mono- and polydisperse soot aggregates, Appl. Phys. B Lasers Opt. 104 (2011) 343–355. https://doi.org/10.1007/s00340-011-4382-x.

[60] M. Saffaripour, K.A. Thomson, G.J. Smallwood, P. Lobo, A review on the morphological properties of non-volatile particulate matter emissions from aircraft turbine engines, J. Aerosol Sci. 139 (2020). https://doi.org/10.1016/j.jaerosci.2019.105467.

[61] B. Giechaskiel, M. Maricq, L. Ntziachristos, C. Dardiotis, X. Wang, H. Axmann, A. Bergmann, W. Schindler, Review of motor vehicle particulate emissions sampling and measurement: From smoke and filter mass to particle number, J. Aerosol Sci. 67 (2014) 48–86. https://doi.org/10.1016/j.jaerosci.2013.09.003.

[62] L. Durdina, B.T. Brem, M. Abegglen, P. Lobo, T. Rindlisbacher, K.A. Thomson, G.J. Smallwood, D.E. Hagen, B. Sierau, J. Wang, Determination of PM mass emissions from an aircraft turbine engine using particle effective density, Atmos. Environ. 99 (2014) 500–507. https://doi.org/10.1016/j.atmosenv.2014.10.018.

[63] L. Liu, M.I. Mishchenko, W. Patrick Arnott, A study of radiative properties of fractal soot aggregates using the superposition T-matrix method, J. Quant. Spectrosc. Radiat. Transf. 109 (2008) 2656–2663. https://doi.org/10.1016/j.jqsrt.2008.05.001.

[64] K. Skorupski, J. Mroczka, N. Riefler, H. Oltmann, S. Will, T. Wriedt, Impact of morphological parameters onto simulated light scattering patterns, J. Quant. Spectrosc. Radiat. Transf. 119 (2013) 53–66. https://doi.org/10.1016/j.jqsrt.2012.12.014.

[65] A. Crayford and M. Johnson and R. Marsh and Y. Sevcenco and D. Walters and P. Williams and S. Christie and W. Chung and A. Petzold and A. Ibrahim and D. Delhaye, SAMPLE III SC. 01-Studying, sAmpling and Measuring of aircraft ParticuLate Emissions III: Specific Contract 01., 2011. https://www.easa.europa.eu/document-library/research-projects/easa2010fc10-sc02.

[66] N.A. Fuchs, On the stationary charge distribution on aerosol particles in a bipolar ionic atmosphere, Geofis. Pura e Appl. 56 (1963) 185–193. https://doi.org/10.1007/BF01993343.

[67] F.-X. Ouf, P. Sillon, Charging Efficiency of the Electrical Low Pressure Impactor's Corona Charger: Influence of the Fractal Morphology of Nanoparticle Aggregates and Uncertainty Analysis of Experimental Results, Aerosol Sci. Technol. 43 (2009) 685–698. https://doi.org/10.1080/02786820902878245.

[68] T.A. Sipkens, J.S. Olfert, S.N. Rogak, New approaches to calculate the transfer function of particle mass analyzers, Aerosol Sci. Technol. 54 (2020) 111–127. https://doi.org/10.1080/02786826.2019.1680794.

[69] M.D. Wilson, D.M. Rocke, B. Durbin, H.D. Kahn, Detection limits and goodness-of-fit measures for the two-component model of chemical analytical error, Anal. Chim. Acta. 509 (2004) 197–208. https://doi.org/10.1016/j.aca.2003.12.047.

[70] R. Dastanpour, S.N. Rogak, Observations of a Correlation between Primary Particle and Aggregate Size for Soot Particles, Aerosol Sci. Technol. 48 (2014) 1043–1049. https://doi.org/10.1080/02786826.2014.955565.

9. Tables and figures

Table 1. Sources and sizes of the soot particles measured in this work. $d_{pp,100}$: mean spherule diameter for soot aggregates with $d_m \approx 100$ nm. CMD: count median diameter (equivalent to geometric mean diameter, GMD, for lognormal data). GSD: geometric standard deviation. MMD: mass median diameter of a lognormal distribution with the specified CMD and GSD neglecting density variation with size.

Source	Name	Fuel	$d_{pp,100}$ [nm]	CMD [nm]	GSD [-]	MMD [nm]
1	Gnome turbine	Jet A-1	20 [a]	40 [b]	1.8 [a]	110
2	Diesel generator	Diesel	-	100	1.6	190
3	Argonaut MISG	Propane	18 [c]	215	1.7	500
4	miniCAST-S	Propane	-	266	1.5	435
5	miniCAST-D	Propane	26 [d,*]	250 [e]	1.6	485
6	miniCAST-A	Propane	-	257	1.5	420

Measurements from [a]Olfert et al. [45]*; [b]Crayford et al.* [65]*; [c]Baldelli et al. [32]; [d] Durdina et al. [40]; [e]this study (Note that Durdina et al. [40] reported 150 nm).*
[*]Reported by Ref. [40] without reference to aggregate size.

946 Table 2. Combined summary of flow conditions for the Argonaut and miniCAST
947 soot generators. miniCAST setpoints D, S, and A refer to the first setpoint
948 characterized by Durdina et al. [40], the FL2 setpoint characterized by Saffaripour
949 et al. [44], and the setpoint that has been used to calibrate the MSS for aviation
950 turbine engine soot, respectively.
951

Setpoint	Flow [SLPM]			
	Propane	Air	Premixed N_2	Post-flame dilution air
Argonaut MISG	0.075	7.5	0	0
miniCAST-D	0.071	1.91	0	9.8
miniCAST-S	0.055	1.6	0	20
miniCAST-A	0.060	1.6	0	20

952

Table 3. MAC model descriptions. Variables such as soot density which were common between models are omitted. DLCA: diffusion-limited cluster aggregation.

Model	Hypothesis tested	Soot morphology	d_{pp}	RI
Mie	None (literature context only)	Volume-equivalent sphere	Fixed	$1.77 + 0.76i$
RDG-0	Null hypothesis for GMM-1 and RDG-3	Non-interacting monomers	Fixed	$1.77 + 0.76i$
GMM-1	Internal light scattering	DLCA aggregate	Fixed	$1.77 + 0.76i$
GMM-2	Monomer–aggregate size correlation	DLCA aggregate	$= f(d_m)$[a]	$1.77 + 0.76i$
RDG-3	Quantum confinement effects	Non-interacting monomers	Fixed	$= g(d_m)$[b]

[a]*Parameterized as a function of d_m using Equation 6; resulting in d_{pp} of 16 to 27 nm for the d_m range 60 to 262 nm (cf. Figure S5).* [b]*Parameterized as a function of d_m following Ref. [33] resulting in RI of $1.66 + 0.75i$ to $1.66 + 0.76i$, as discussed in the text.*

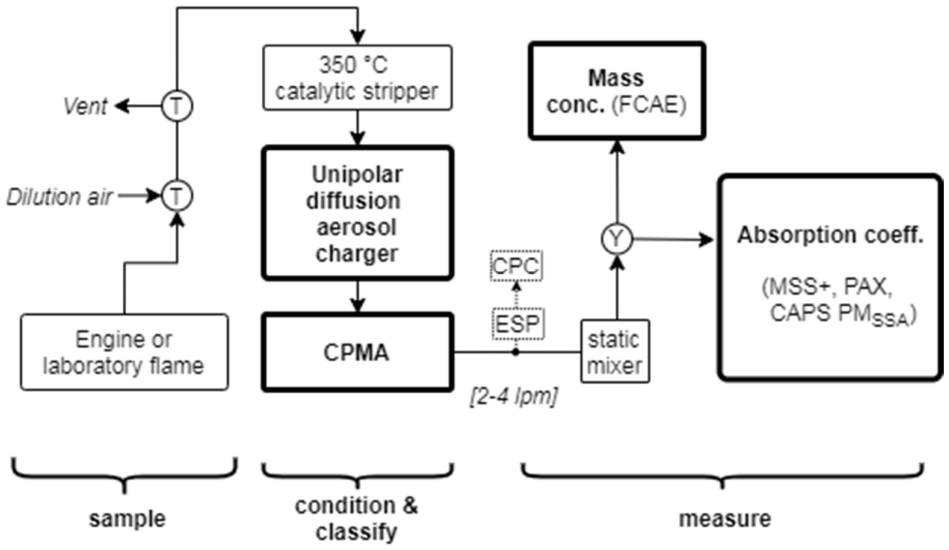

Figure 1. Experimental setup. A heated line (60 °C) was used between the engine or laboratory flame and the dilution stage. CPMA: Centrifugal particle mass analyzer. CPC: condensation particle counter. ESP: electrostatic precipitator. FCAE: faraday cup aerosol electrometer. MSS, PAX, and CAPS PM_{SSA}: instruments used for absorption coefficient measurements (see Table S1).

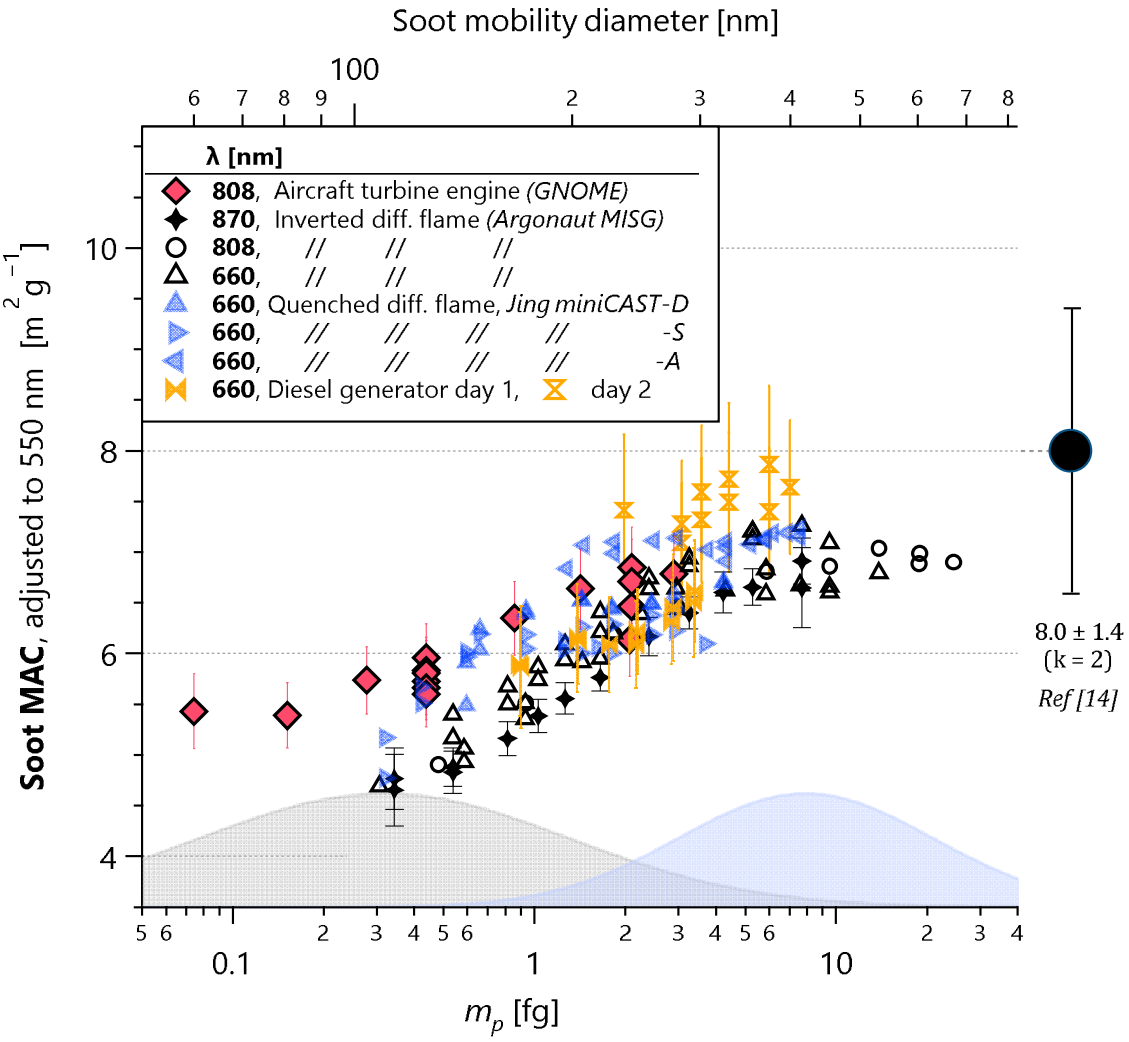

Figure 2. Size-resolved MAC for the Gnome aviation turbine engine, Diesel generator, Argonaut MISG, and the miniCAST-A, -D and -S setpoints. The measurements represent three different instruments (Table S1) adjusted to a common wavelength of 550 nm using Equation 2. The grey and blue shaded regions illustrate lognormal mass distributions from Table 1, with arbitrary vertical scale, of the Gnome aviation turbine engine (which produced the smallest soot particles) and the miniCAST-A setpoint (which produced the largest particles), respectively. Some error bars are omitted for clarity.

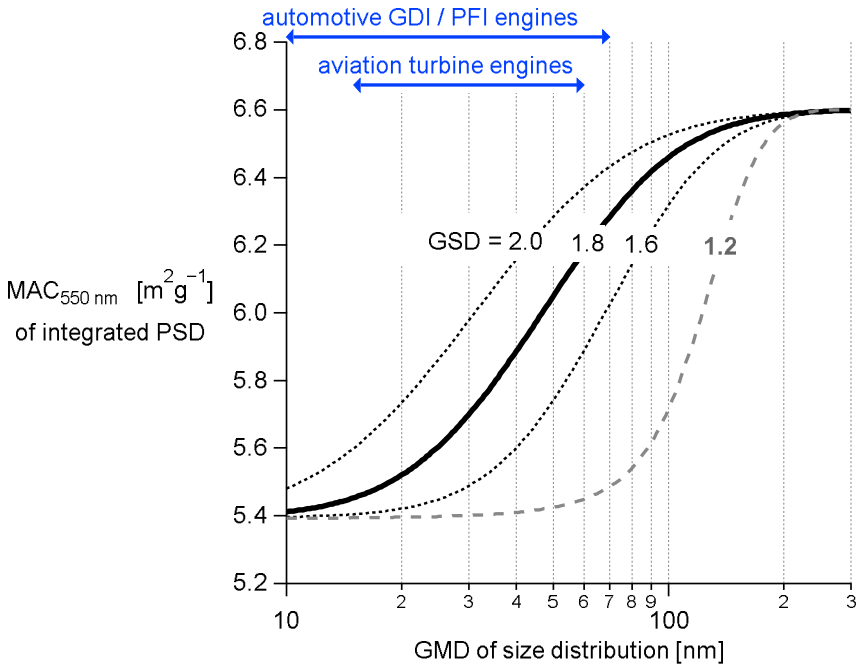

981

982 Figure 3. Size-resolved MAC from the sigmoidal fit to Gnome data in Figure 2
983 weighted by lognormal distributions spanning the GMD range reported previously
984 for aviation turbine engine [60] and automotive engine [61] soot particles. The
985 GSDs of 2.0, 1.8, and 1.6 represent plausible size distributions; the GSD of 1.2
986 represents the narrower distributions produced by the CPMA. If a MAC
987 corresponding to large particles is assumed for small soot particles, the resulting
988 positive bias in calculated mass concentration may be as high as 18%.

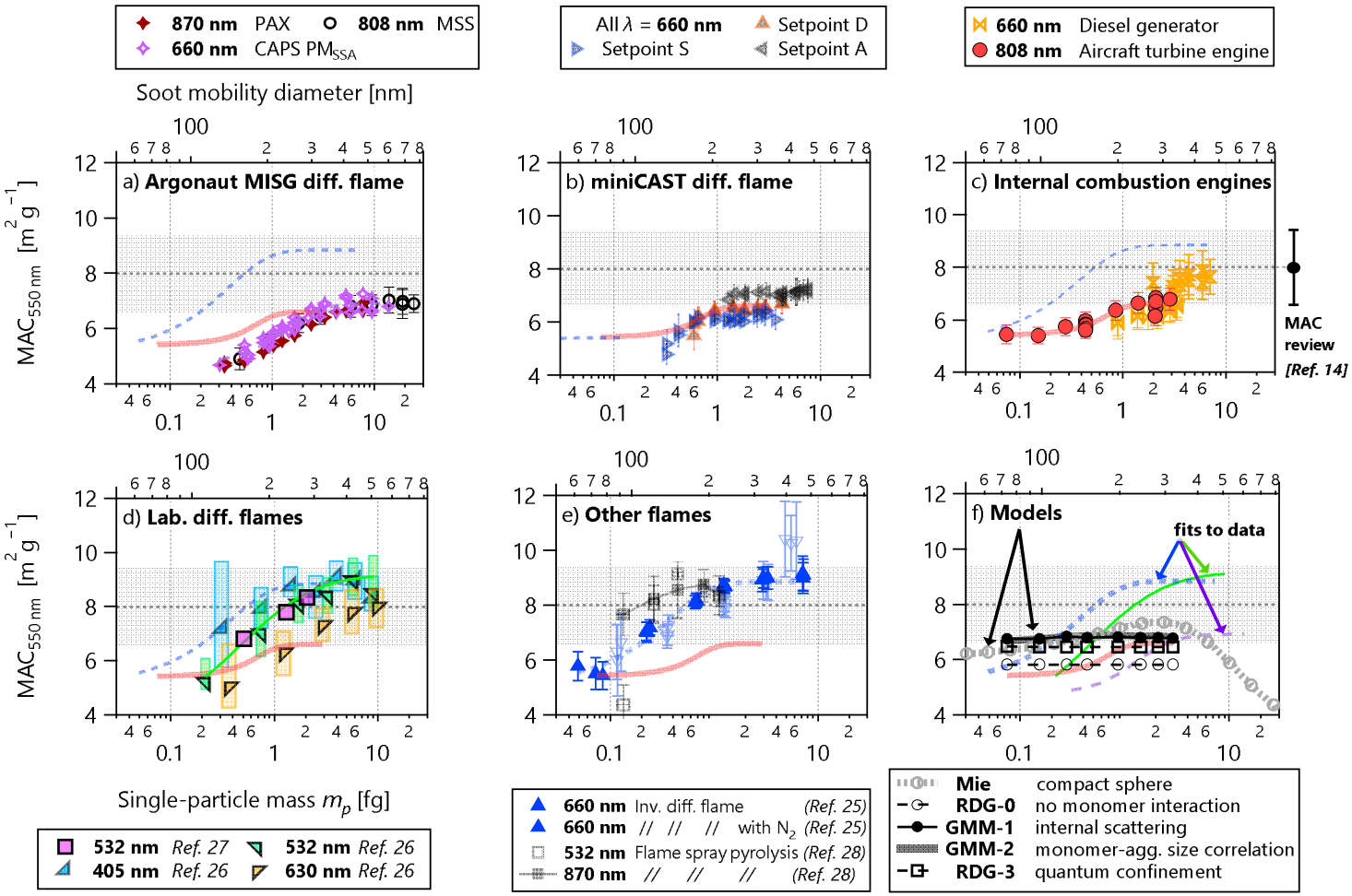

Figure 4. Size-resolved MAC for the samples measured in this study (a-c) and literature [25–28] (d-e), and modelled in this study (f). In (f), Model RDG-0 represents the null hypothesis; Models GMM-1, GMM-2, and RDG-3 represent the hypothetical causes of size-dependent MAC discussed in the text; and the (unphysical) Mie model is included for context. Grey shading shows the mean MAC_{550nm} and $k = 2$

993 uncertainty reported by recent size-integrated studies [14]. All fits are to guide the eye and are reproduced in (f), some fits are
994 reproduced in (a)-(e) to facilitate comparison. The vertical bars in (d) represent upper and lower quartiles of the compiled data set of
995 Forestieri et al. [26]; all other error bars represent standard errors. All data have been harmonized to $\lambda = 550$ nm assuming AAE = 1.
996

S1. Supplementary information

This supplementary information contains:

- Additional text on data analysis
- Additional tables from the literature review of MAC measurements
- Additional visualizations of our analysis and results

S1.1. Data inversion

We performed two data inversions based on the mass distribution of the CPMA classified particles estimated by its transfer function, as well as a simplified inversion independent of this mass distribution. The simplified iterative inversion estimated the average single-particle mass classified by the CPMA, $\overline{m_p}$ by iteratively solving

$$\overline{m_{p,k+1}} = \overline{m_{p,k}} \times F\left(d_m\left[\overline{m_{p,k}}\right]\right) \quad \text{S1}$$

Where $\overline{m_{p,k}}$ and $\overline{m_{p,k+1}}$ are initial and improved estimates of the average single-particle mass classified by the CPMA $\overline{m_p}$, F is the Fuchs charging model [66] used to predict the average charge of a particle with mobility diameter d_m, which is estimated from the particle mass m_p using the universal mass-mobility relationship described below. The value of $\overline{m_{p,k}}$ is taken as the mass of a singly-charged particle initially and the equation is iterated until the solution converges. This simple approach is hereafter referred as the iterative-average-charge inversion.

Under our conditions[1], the Fuchs charging model resulted in a curve which could be parameterized as

$$\bar{q} = 6.4168 \cdot m_p^{0.4204} + 0.4587 \qquad \text{S2}$$

Where $\bar{q}$ is the average number of charges on a particle of mass m_p (in fg) charged by the UDAC at an ion·charge product of 10^{13} ions·s/m^3.

The second and third data inversions were based on the mass distribution of the classified particles estimated by the CPMA transfer function as follows. For each soot source, we represented the particle population using lognormal mobility diameter d_m distributions described by the measured geometric count mean diameters CMD and geometric standard deviations GSD of each source (Table 1). The charge distribution $q(d_m)$ on these particles after the UDAC was predicted using the Fuchs model [66] using a dielectric constant of 13.5. This dielectric constant is an average of the range used by Ouf and Sillon [67] for soot, and our results were relatively insensitive to this assumption. The lognormal distributions were then converted to mass distributions based on the universal mass-mobility relationships of soot described by Olfert and Rogak [58] (power-law prefactor of 0.1169; exponent 2.48). The transport of this mass distribution through the CPMA was predicted using CPMA transfer functions calculated using the finite-difference method outlined by Sipkens et al. [68]. The CPMA output mass distribution was then calculated by combining the input mass distribution with the charge distribution and transfer function. This inversion assumes that the charge distribution is approximately constant across the narrow width of the CPMA transfer function for each particle charge. The predicted output mass distribution was then used to calculate the relative number of particles of each charge state q exiting the CPMA at a given setpoint. Negligible number fractions (n_q<0.01%) were discarded.

[1] Aerosol pressure and temperature of 101,325 Pa and 298.15 K, respectively, as well as assuming the soot particles follow the mass-mobility relationship established by Olfert and Rogak [58].

The mass distribution results (i.e. the calculated relative number of particles of each charge state exiting the CPMA) were used to estimate the relationship of MAC to single particle mass using two independent methods. In the first method, we calculated the average mass of the classified particles ($\overline{m_p}$) based on the estimated mass distribution at each test point using

$$\overline{m_p} = \sum_{q=1}^{q_{\max}} m_q n_q \qquad \text{S3}$$

Where n_q and m_q are the number fraction and single-particle mass of particles with charge q classified by the CPMA, respectively. These quantities are summed from $q = 1$ to $q_{\max}$, where $q_{\max}$ is the maximum number of charges where n_q was non-negligible, as defined above. We then attributed the MAC calculated with Equation 1 to particles of mass $\overline{m_p}$. This first method, referred to as the average-mass inversion, implicitly assumes that the mass distribution of the CPMA classified particles is narrow[2] (such that most of the particles contributing to $\overline{m_p}$ have similar mass) and that the MAC of the individual particles is constant over this narrow distribution.

In the second method, also based on the estimated mass distribution of the CPMA classified particles, we used Equation 1 to describe each unique particle mass m_j as having its own MAC, MAC_{mj} and its own mass loading $M_{PM,j} = N_j m_j$:

$$\mathrm{MAC}_{m_j} = \frac{B_{\mathrm{abn},j}}{N_j m_j} \qquad \text{S4}$$

[2] The width of the classified mass distribution is a function of the combined widths of the particle charge distribution, CPMA transfer function and polydispersed aerosol.

Where N_j is the total number concentration of particles with mass m_j and charge j. Note that a particle with mass m_j might be transmitted by the CPMA as a singly charged particle, doubly charged particle, or other multiply charged particle $\left(m_j = m_1/1 = 2m_2/2 = qm_3/q\right)$. This fact can be captured using a system of equations and simultaneously solved to determine MAC_q for all m_q.

In order to construct a system of equations that is over-constrained (more measurement points than degrees of freedom), we first consolidated the mass fractions of the CPMA classified particles ($f_{i,j} = n_{i,j}m_j / \sum_j n_{i,j}m_j$) into a matrix of common mass bins (columns) for all test points (rows), then consolidated this matrix into a number of log-spaced mass bins that was a factor of 2 to 4 smaller than the number of test points. The consolidated matrix was further simplified by (a) removing mass bins (i.e. columns of matrix) that were often empty (i.e. $f_{i,j} > 0.01$ in fewer than three bins at a given value of j) and (b) by removing test points where the mass distribution was no longer adequately represented (i.e. $\sum_j f_{\mathrm{i},j} < 0.99$) after this consolidation process. The second criteria was rarely implemented and was mostly applied to samples that had multiple mass bins removed for not meeting criterion (a) due to not overlapping in the mass domain of at least two other samples.

The consolidated matrix can be written by defining $f_{i,j}$ as the mass fraction of particles with mass m_j at test point i as:

$$\begin{bmatrix} f_{1,1} & \cdots & f_{1,j} \\ \vdots & \ddots & \vdots \\ f_{i,1} & \cdots & f_{i,j} \end{bmatrix} \begin{bmatrix} \mathrm{MAC}_{m_1} \\ \vdots \\ \mathrm{MAC}_{m_j} \end{bmatrix} = \begin{bmatrix} \mathrm{MAC}_1 \\ \vdots \\ \mathrm{MAC}_i \end{bmatrix} \quad \text{S5}$$

which is a system of equations that represents the measured MAC_i as a sum of the (potentially) different MAC_{m_j} for each single-particle mass bin m_j. This system of equations was solved by applying least-squares minimization inversely weighted by the standard deviation of the measured MAC at each test point plus 1% of the

same value. The 1% offset was included in the fit normalization to reduce the preferential weighting that least-squares minimization inherently places on the largest values measured and follows previous recommendations [69]. This second method based on the estimated mass distribution is referred to as the system-of-equations inversion, and its uncertainties for a k=1 coverage factor were determined by bootstrapping (repeatedly and randomly sampling a subset of the complete data set).

S1.2. Validation of data inversion

Figure S1. shows that the three data inversions (iterative average charge, average single-particle mass or system-of-equations inversion), used to determine the relationship of MAC to individual particle mass, produce similar results. The figure uses data from the CAPS PM_{SSA} monitor measuring MISG soot as an example.

The iterative average charge inversion agreed closely with the average single-particle mass inversion for all test points, despite its implicit assumptions that the sampled particle size distribution and the CPMA transfer function may be neglected. This unexpected agreement can be understood by reference to the more detailed calculation of the m_p and charge distribution exiting the UDAC–CPMA. The distribution of total charge as a function of m_p was approximately lognormal (Figure S2 and Figure S3) due to the large number of charges per particle imparted by the unipolar charger in the UDAC. Our observed agreement implies that this charge distribution played the major role in determining the average m_p, while the sampled particle size distribution and CPMA transfer function played minor roles. At present, this conclusion is specific to the conditions of our study; further investigation is required to validate these implications and identify limitations of the iterative average charge inversion.

Finally, the system-of-equations inversion showed a similar trend as the average single-particle mass inversion in Figure S1.. This agreement confirms that the

1127 average-mass inversion, and its associated assumptions (as previously described)
1128 were valid for the data collected in this study. In the following discussion, we focus
1129 on the results produced by the average-mass inversion because the system-of-
1130 equations inversion involved grouping the data in the m_p dimension in order
1131 produce an over-constrained system where the system-of-equations could be
1132 fitted successfully.

1133

1134 ### S1.3. Fit function applied to size-dependent MACs

1135 In Figure 3 and Figure 4, we used the error function to describe our MAC
1136 observations, with lower limit *a,* upper limit *b*, and abscissa-offset and scaling
1137 parameters *c* and *d*:

$$\mathrm{MAC} = a + (b - a)\left[\frac{1}{2} + \frac{1}{2}\mathrm{erf}\big(c \log m_p - d\big)\right] \qquad \text{S6}$$

1138

1139 It may be expected that $a \approx 4\ \mathrm{m^2 g^{-1}}$ (the MAC of incipient soot particles described
1140 by Wan et al. [34]), $b \approx 8 \pm 0.7\ \mathrm{m^2 g^{-1}}$ (the MAC of mature soot reviewed by Liu et
1141 al. [14]) and that c and d vary slightly according to the discussion in the main text.
1142 However, the available data did not allow this expectation to be rigorously tested.

1143 ### S1.4. Single-scattering albedo (SSA)

1144

1145 Our CAPS $\mathrm{PM_{SSA}}$ measurements provide single-scattering albedos (SSAs) at 660 nm
1146 for each size-resolved MAC test point. Figure S7 and Figure S8 show these SSAs
1147 plotted as a function of average single-particle mass m_p and as a function of MAC,
1148 respectively. In Figure S7, the SSA generally increases slightly from 0.12 to 0.22 as
1149 m_p increases from 0.3 fg to 10 fg. The SSA trend is not clearly sigmoidal as was the
1150 case for MAC, potentially because the SSA is influenced more strongly by
1151 morphology than the MAC [16,18]. Also, the SSA trend shows less variability than
1152 the corresponding trend of MAC versus m_p discussed in the main text, potentially
1153 because the SSA trend reflects increasing particle size parameter x rather than a

changing MAC [15]. Notably, the trend for the Argonaut MISG and the diesel engine soot indicate higher SSAs for larger particles than the other sources. This may reflect more-compact soot particles being emitted from these sources, relative to the others.

In Figure S8, the 660 nm SSA is plotted against the MAC reported in the manuscript. No clear trend is seen in the data. The SSA was more strongly associated with particle size than with the measured MAC.

S1.5. Supplementary tables

Table S1. Instruments used to measure in situ aerosol light absorption in this work. CAPS PM_{SSA}: Cavity attenuation phase shift—particulate matter single scattering albedo; MSS: Micro soot sensor; PAX: photoacoustic extinctiometer.

Instrument	**λ [nm]**	**Measurement principle**	**Calibration source**
CAPS PM_{SSA}	660	Extinction minus scattering	$(NH_4)_2SO_4$
MSS	808	Photoacoustic	MISG soot
PAX	870	Photoacoustic	Graphitic nanoparticles and $(NH_4)_2SO_4$

Table S2. Experimental conditions of single-particle-mass- or size-resolved MAC measurements in the literature. The APM (Aerosol Particle Mass Analyzer) in this table is analogous to the CPMA. The expression "DMA–APM+CPC" (or "DMA-CPMA+CPA") describes the use of a DMA to size-classify particles that are then counted by a CPC, then multiplied by the average single-particle mass measured by an APM–CPC (or CPMA-CPC) experiment, which is sometimes called an effective density measurement.

Study	Particle charging	Particle classification	Absorption measurement, B_{abn}	Mass concentration measurement, M_{PM}
This work	Highly charged (UDAC)	CPMA	Photoacoustic (2 instruments) and extinction-minus-scattering (CAPS PM_{SSA})	CPMA–electrometer
Khalizov 2009 [26]	Equilibrium (^{210}Po)	DMA–CPMA	Extinction-minus-scattering (house-made)	DMA–APM+CPC
Dastanpour 2017 [24]	Highly charged (UDAC)	CPMA	Extinction-minus-scattering (CAPS PM_{SSA})	CPMA–electrometer
Forestieri 2018 [25]	Equilibrium (X-ray)	DMA and DMA–CPMA	Photoacoustic (3 instruments) and extinction-minus-scattering (CAPS PM_{SSA})	DMA–CPMA+CPC
Kholghy and DeRosa 2020 [27]	Equilibrium (X-ray)	DMA	Photoacoustic (DMT PAX)	DMA–APM+CPC

.

S1.6. Supplementary figures

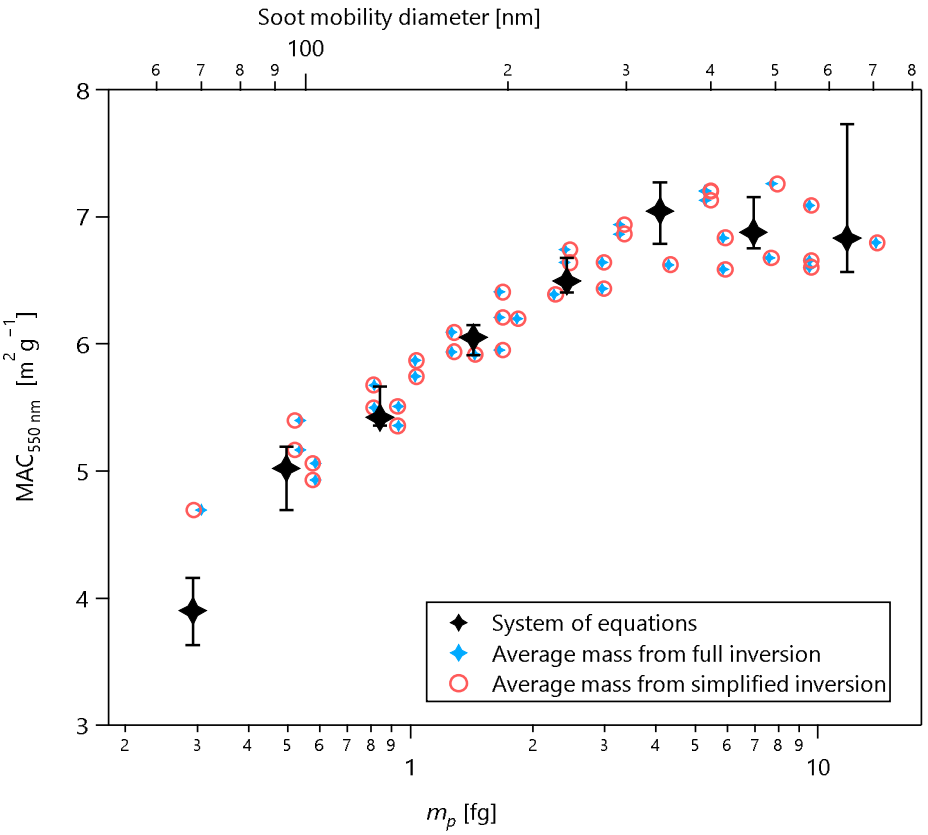

Figure S1. MAC_{550nm} calculated using the three inversion methods for the CAPS PM_{SSA} data measured at 660 nm. Some error bars are omitted for clarity. Fewer data points are available through the system of equations for the statistical reasons described in the text. Therefore, other figures in this work used the second data set (average mass from full inversion).

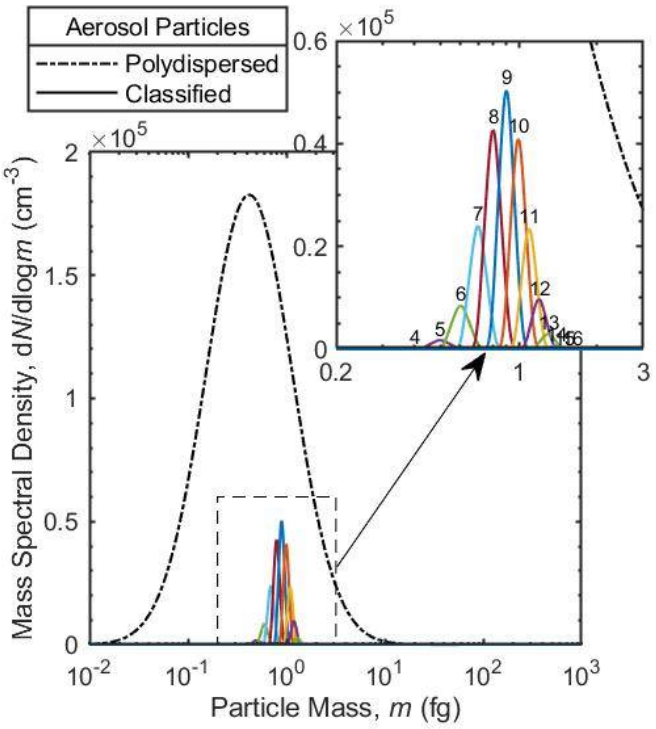

Figure S2. A representative mass distribution for particles transmitted through the CPMA after the UDAC. The example shows the input mass distribution (black line) and output mass distributions of particles with $1 < q < 15$ for miniCAST-D particles with $m/q = 0.1$ fg/e at a CPMA resolution of 3. The sum of all outputs may be described as a Gaussian distribution.

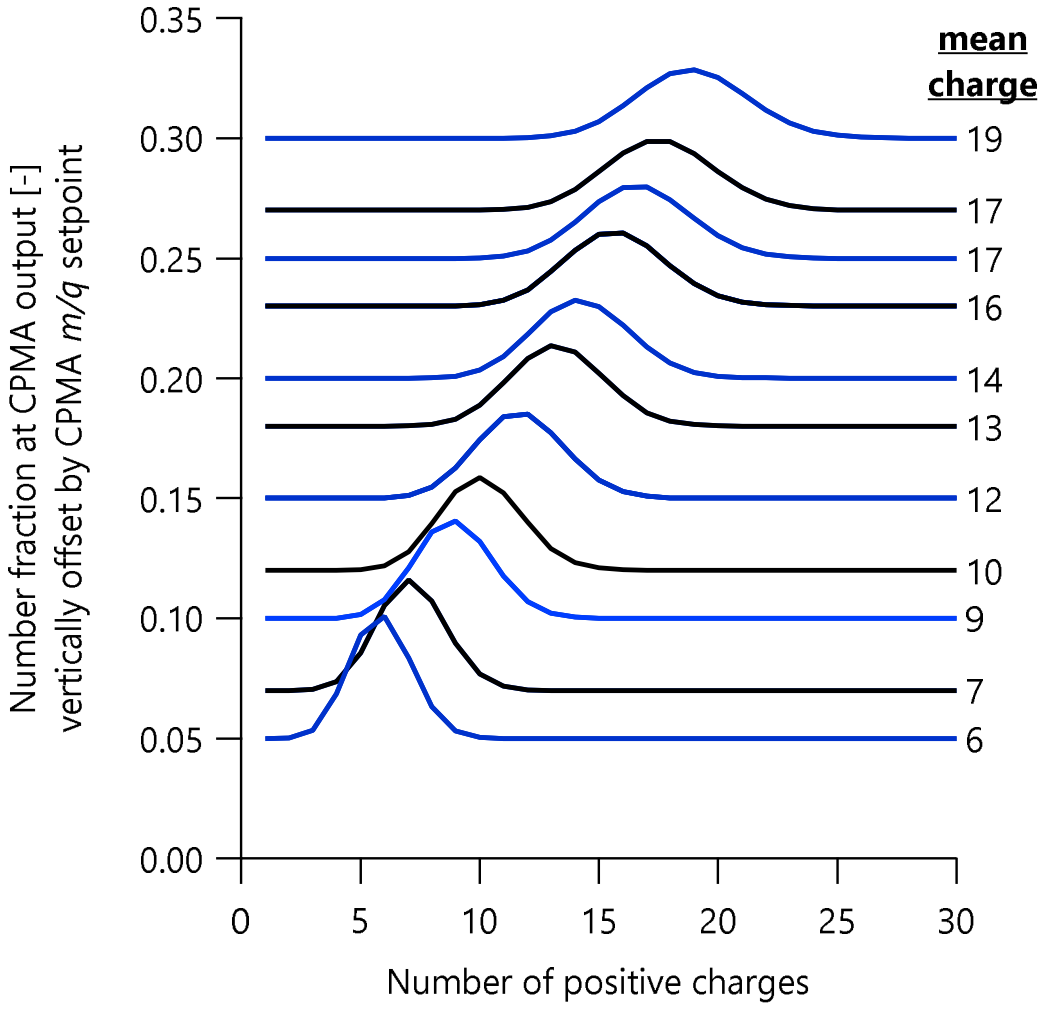

Figure S3. Similar to Figure S2 but for all CPMA setpoints in the Diesel generator experiment. The CPMA setpoint is illustrated by the intercept of the curves on the ordinate axis and is between 0.05 and 0.30 fg/e. The probability distribution of charges is shown by each curve. The mean charge is shown by the values on the right.

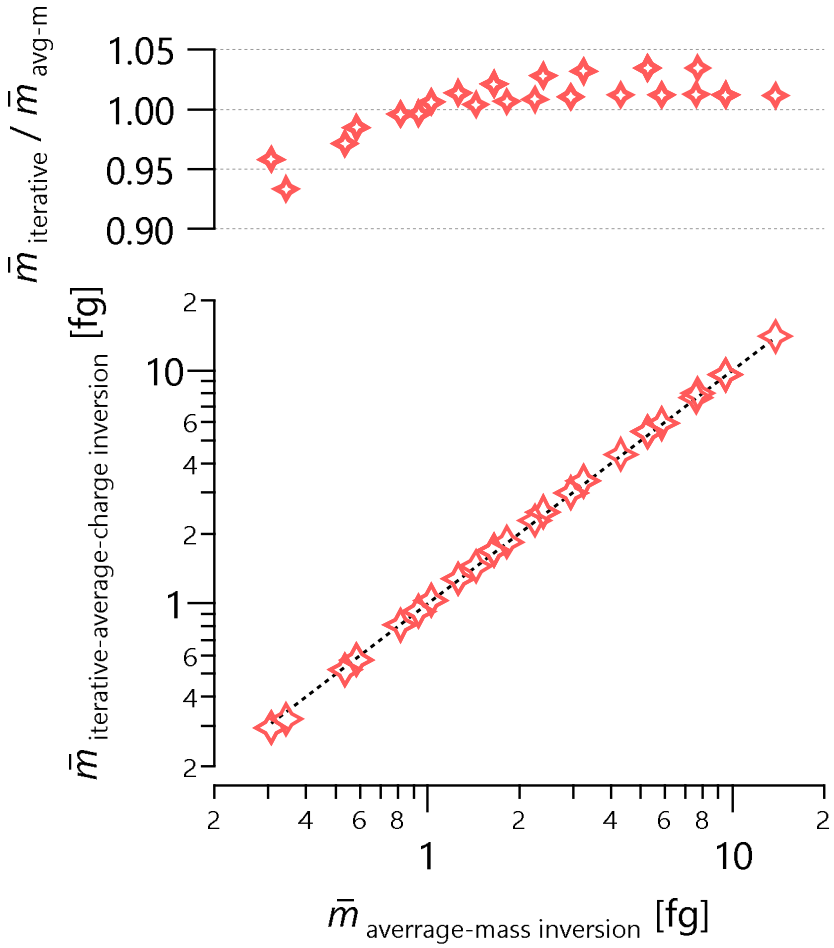

Figure S4. Comparison of the mean CPMA-transmitted single-particle mass from the iterative-average-charge method and the average single-particle mass methods.

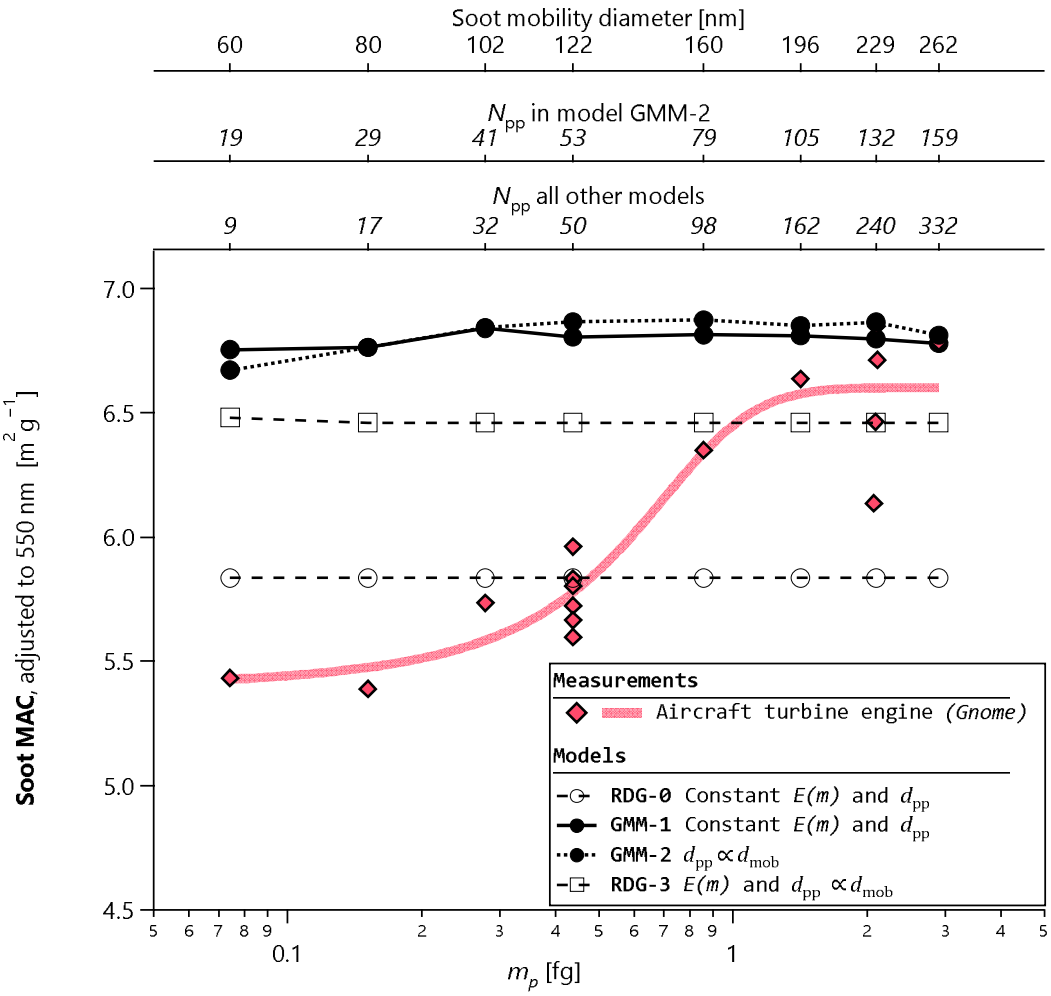

Figure S5. Measured and modelled size-resolved MACs for the Gnome aviation turbine engine. The fit to the measurements highlights the observed sigmoidal trend. We modelled 3 hypotheses for size-dependent soot properties. The null hypothesis assumes DLCA aggregates of constant d_{pp} and RI. The correlation model implements the correlation of d_{pp} with d_m (and m_p) observed previously [25,58,70]. The graphitic-shell model extends the correlation model to hypothesize that the extreme curvature of smaller soot particles makes them less graphitic. Finally, the model of Kelesidis and Pratsinis [33] is plotted for comparison, although it does not represent the d_{pp} of this engine.

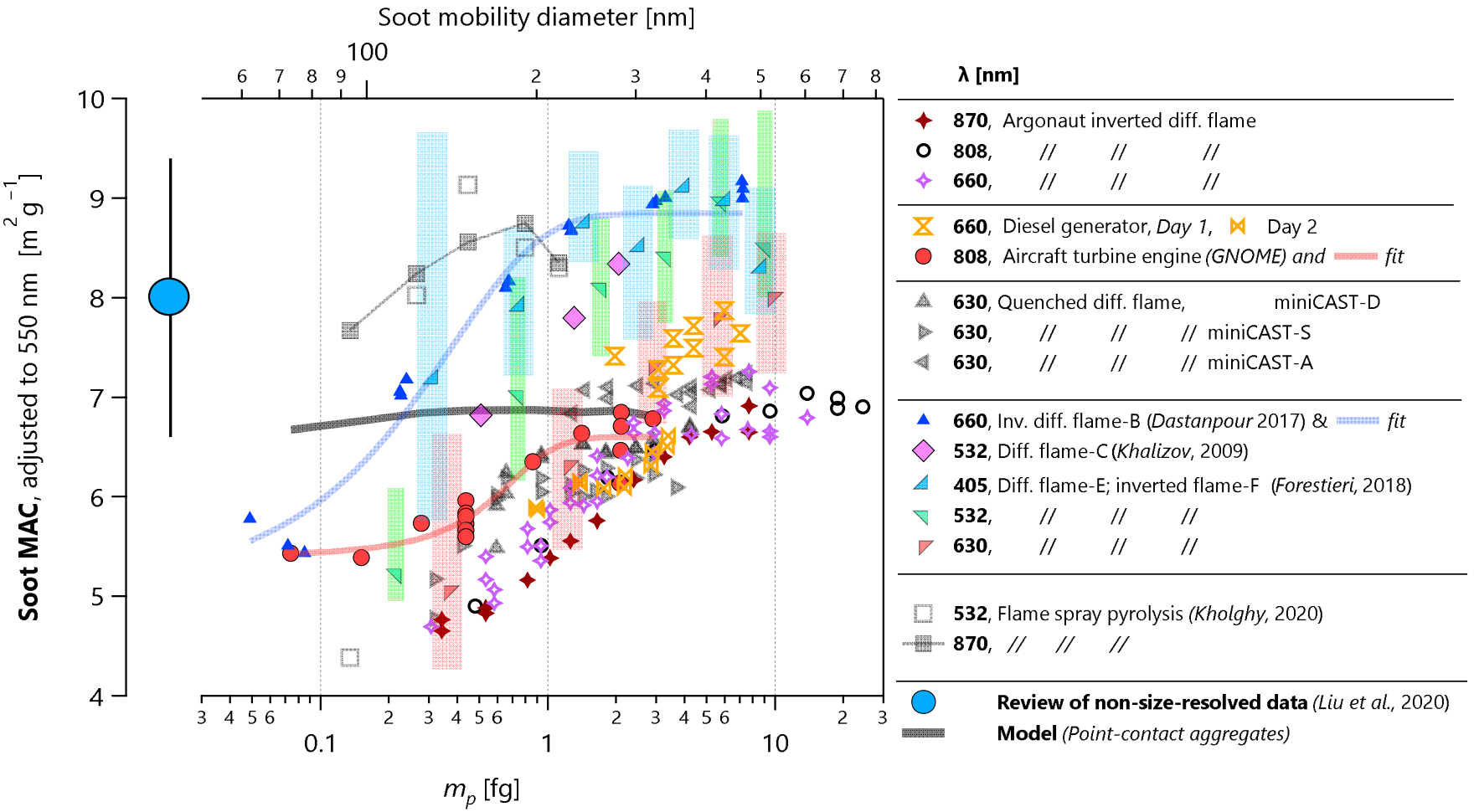

Figure S6. Similar to Figure 4 but with data overlaid on a single panel.

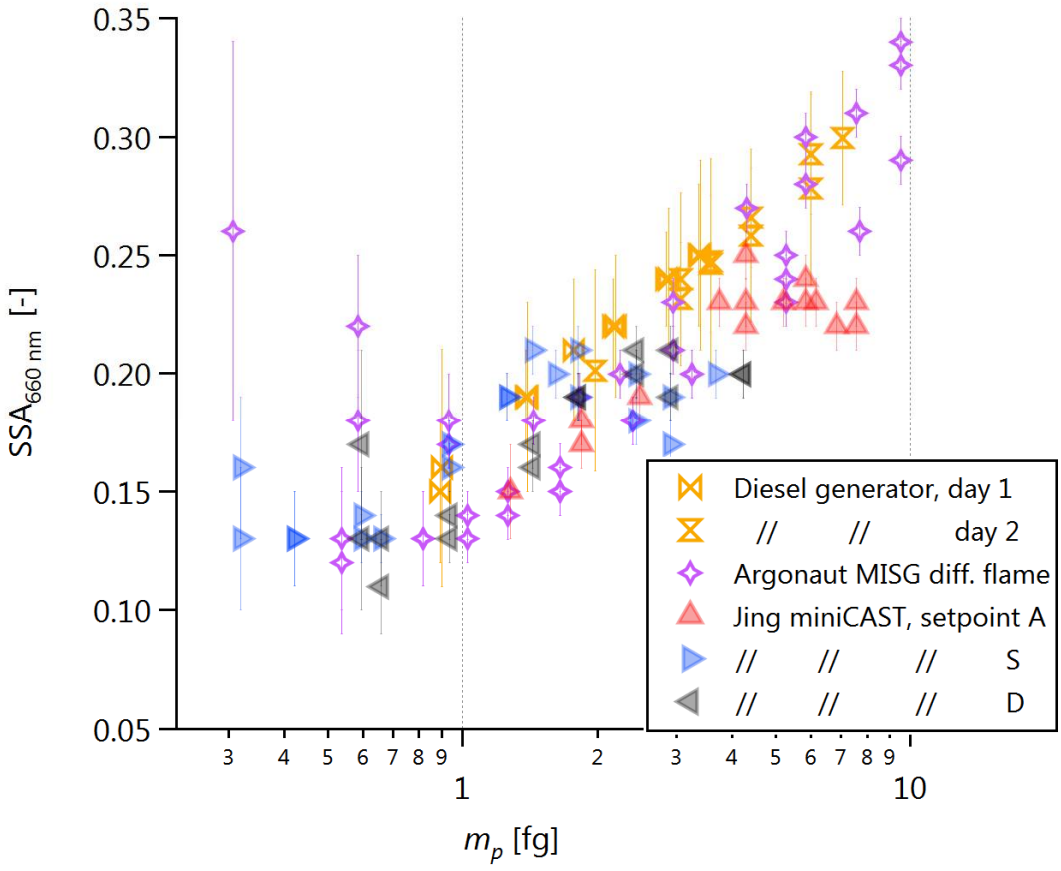

Figure S7. Single scattering albedo (SSA) versus single-particle mass for the 660 nm CAPS PM_{SSA} data.

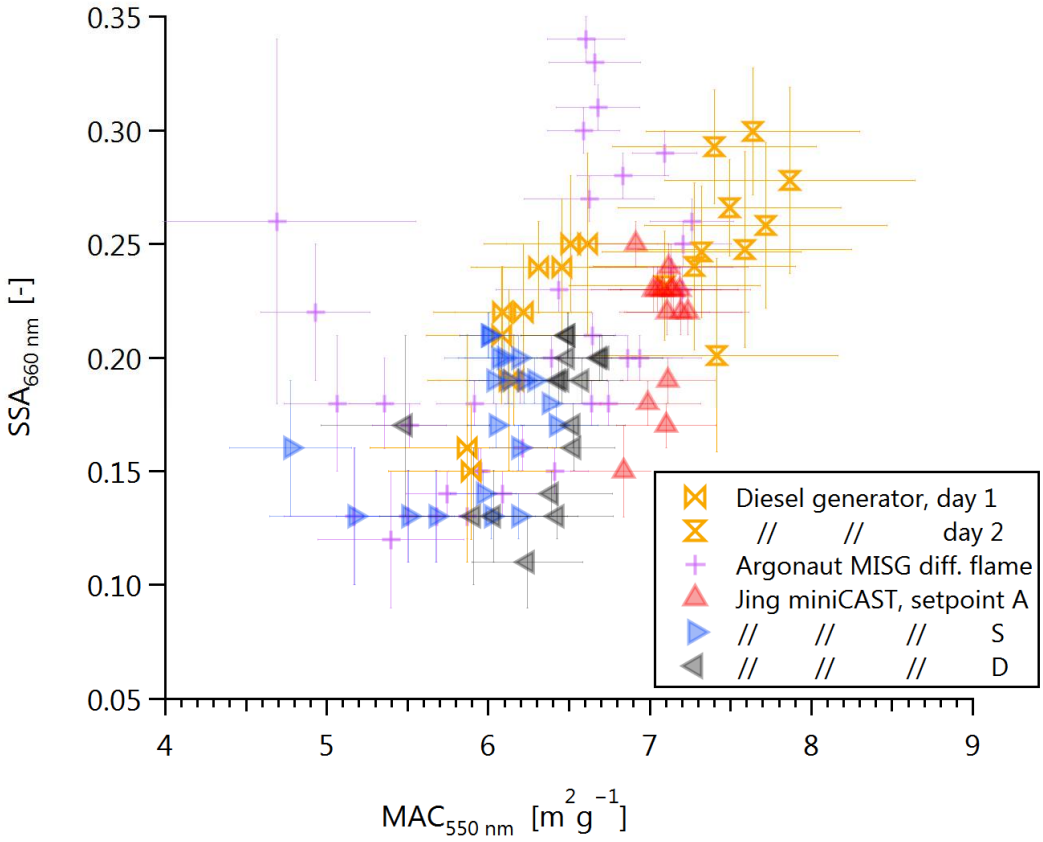

Figure S8. Single scattering albedo (SSA) versus MAC_{550nm} for the 660 nm CAPS PM_{SSA} data.

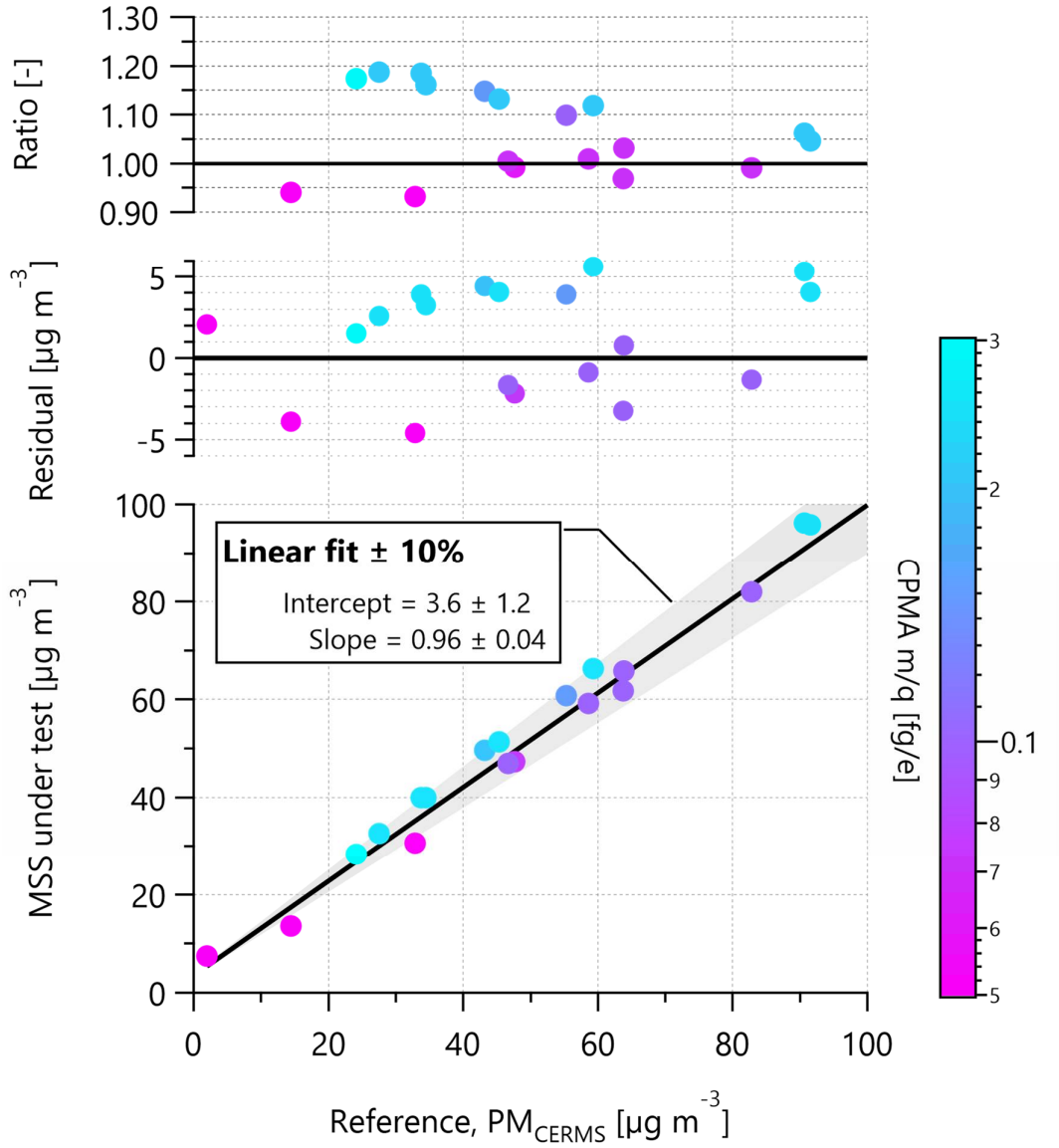

Figure S9. Calibration of the MSS used in this study using the Gnome data shown in Figure 2, Figure S5, and other figures. The size-resolved MAC signal results in a scatter of only approximately 10% in the calibration scatterplot and residuals. However, this scatter is systematic enough to allow for the size-resolved MAC to be inferred, as discussed in the manuscript.